Title
2-D MR Spectroscopy Combined with 2-D/3-D Spatial Encoding

Journal
EMAGRES, 5(1)

ISSN
2055-6101

Authors
Thomas, M Albert
Iqbal, Zohaib
Sarma, Manoj K
et al.

Publication Date
2016

DOI
10.1002/9780470034590.emrstm1459

Peer reviewed

Chapter 30

Two-Dimensional NMR Spectroscopy Plus Spatial Encoding

M. Albert Thomas[1], Zohaib Iqbal[1], Manoj K. Sarma[1], Rajakumar Nagarajan[1], Paul M. Macey[1], and Amir Huda[1,2]

[1] *University of California, Los Angeles, CA, USA*
[2] *California State University, Fresno, CA, USA*

30.1	Introduction	495
30.2	Single-voxel-based 2D MRS	497
30.3	Echo-planar Correlated and J-resolved MRSI	506
30.4	Accelerated Echo-planar J-resolved MRSI with Nonuniform Undersampling and Compressed Sensing	514
30.5	Prior-knowledge Fitting for Metabolite Quantitation	515
30.6	Future Directions: Clinical Applications	517
	Acknowledgments	517
	References	517

Handbook of Magnetic Resonance Spectroscopy In Vivo: MRS Theory, Practice and Applications.
Edited by Paul A. Bottomley and John R. Griffiths
 ISBN: 978-1-118-99766-6
Also published in eMagRes (online edition)
DOI: 10.1002/9780470034590.emrstm1459

30.1 INTRODUCTION

It is now almost three decades since one-dimensional (1D; in the chemical shift spectral domain) single-voxel (SV)-based magnetic resonance spectroscopy (MRS) was introduced in the clinical setting.[1–3] While it has become an integral part of the diagnostic tools in the clinic for some physicians and selected medical centers, it is still considered by others as an 'investigational technique'.[1,3] 1D SV-MRS has developed to a point where the five major cerebral metabolites, myo-inositol (mI), total choline (Cho), total creatine (Cr; phosphorylated plus unphosphorylated), glutamine/glutamate (Glx), and *N*-acetyl aspartate (NAA), are identified and quantified accurately with prior-knowledge fitting algorithms such as *LC Model*, *JMRUI*, and others (see Chapters 18, 19, and 20).[4–6] Acquisition times have also been accelerated by stronger gradients, and we have arguably now reached a plateau in terms of what can be further extracted from the 1D technique.[1]

Beyond the five main cerebral metabolites, approximately 25 others that have been detected in human brain are not commonly assessed for several reasons.[6] Some are difficult to detect because they have a weak signal (low concentration or fewer hydrogen

nuclei) and/or many overlapping peaks, for example, *N*-acetylaspartylglutamate (NAAG), aspartate, taurine (Tau), *scyllo*-inositol, betaine, ethanolamine, purine nucleotides, histidine, glucose, and glycogen. Others require the use of 'special techniques' to tease them out because they are obscured by much larger overlapping signals, for example, glutathione and γ-aminobutyric acid (GABA).[1–7] Yet others such as β-hydroxy-butyrate, acetone, phenylalanine, galactitol, ribitol, arabitol, succinate, pyruvate, alanine, glycine, and threonine are detected only when levels are elevated under abnormal or pathological conditions in various disorders. In addition, some exogenous compounds that cross the blood–brain barrier such as ethanol and methylsulfonylmethane can also be detected by proton MRS.[8–10]

The limitations of the 1D SV-MRS methods of yesteryears still remain to a certain extent.[1–3,7] Overlapping of spectra due to the chemical shifts of metabolites keeps us from identifying the ones with fewer hydrogen protons and/or lower concentrations. Furthermore, an inability to separate J-coupling from chemical shift leads to assignment problems that hinder the identification and quantification of metabolites.[11,12] One could, in principle, move to higher main magnetic field strengths (B_0) to better resolve the peaks and reduce the overcrowding, as the relative width of the multiplets in ppm varies inversely with B_0.[13] However, currently 3 T remains the practical limit in the clinical setting.[3]

The 'special techniques' noted above for teasing out signal information are often called *homonuclear spectral* or *J-difference editing techniques*.[14,15] They exploit the J-coupling between coupled spins by selectively perturbing particular resonances on alternate acquisitions during a spin-echo sequence. J-coupling results in multiplet signals with distributed peak intensities (heights) over several peaks, leaving a broader footprint along the chemical shift axis. For example, observing GABA, whose concentration is only 1 mM in the human brain, is difficult because the signal at 3.0 ppm is coupled to the 1.9 ppm peak and overshadowed by large signals from NAA, Glx, and Cr. A frequency-selective pulse, which only directly affects those signals close to 1.9 ppm, can be added to the point-resolved spectroscopy sequence (PRESS). The homonuclear radio frequency (RF) pulse will also have an indirect effect on GABA signals at 3.0 ppm because of the coupling, but not on the other uncoupled signals. If alternate experiments are performed with and without this frequency-selective pulse, the difference will give a spectrum that only contains the signals affected by the selective perturbation.[14,15]

There are a couple of obvious drawbacks to this technique.[14–17] One is that only one metabolite is optimized at a time (assuming that the multiplets of the J-coupled metabolites are well separated). The second disadvantage is the requirement for subtraction to remove the strong overlapping signals, which makes the technique highly vulnerable to subject movement and to instrumental factors, etc. that can introduce artifacts into the spectrum.[16,17] Mescher *et al*. proposed a different metabolite-editing technique based on subtraction of two measurements, called *MEGA* (*Mescher–Garwood*) that can be combined with the two popular SV-MRS techniques, STEAM (stimulated acquisition mode), and PRESS[18–20] (see Chapter 7). Optimized MEGA-editing sequences have also been proposed recently.[21,22] These newer experimental techniques are inherently preferable because they utilize multiple quantum coherences to suppress overlapping signals in a single scan.[23,24]

Beyond the problems noted above, it has become desirable over the years to obtain multivoxel information in a reasonable amount of time.[25–27] Chemical shift imaging (CSI) using 1D MRS has helped satiate this appetite somewhat but it is performed with sequences using long echo times (TEs) and hence incurs partial loss of those cerebral metabolites that have low transverse relaxation times (T_2s).[27–30] On the other hand, multidimensional/multivoxel MRS imaging (MRSI) techniques tackle these problems head-on during acquisition by unambiguously resolving many overlapping peaks nonselectively through the addition of spectral dimensions, while postprocessing schemes such as Profit deal with quantification (see Chapter 20).[31–36] These approaches have opened up the application of MRS to many fields, and this will lead to new paradigms in the coming decades.

It is important to note that while multidimensional techniques have been the mainstay in chemistry and biochemistry for decades, the road to bringing multidimensional spectroscopy from in vitro to in vivo applications has been difficult, primarily because of two major challenges: the B_0 field strength and acquisition times. However, current methodologies have, at least in part, addressed these problems, and state-of-the-art techniques using clinical MRI scanners have improved signal-to-noise ratios (SNR) and reduced acquisition times to clinically practical durations.[11,12]

Currently, at least 15 cerebral metabolites can be identified and quantified using two-dimensional (2D) localized correlated spectroscopy (L-COSY), which combines the original COSY sequence described by Aue *et al*.[37] and postprocessing algorithms developed at the University of California in Los Angeles.[35,38] A tool that can bring so much additional information surely must increase our diagnostic and patient management capabilities in the clinic. This journey to the state-of-the art today is described below.

30.2 SINGLE-VOXEL-BASED 2D MRS

30.2.1 2D L-COSY: Theory

Figure 30.1 shows the 2D L-COSY sequence that was implemented on a 1.5 T MRI/MRS scanner in 2001, where a combination of three slice-selective RF pulses (90°–180°–90°) enabled the localization of a volume of interest (VOI) in a single shot.[38] After the formation of the Hahn spin echo using the first 90° and 180° RF pulse pair, an incremental period for the second spectral dimension (t_1) was inserted immediately. The last slice-selective 90° RF pulse acted also as the coherence transfer pulse, critical for recording the 2D spectrum.[37,38] To remove unwanted coherences, this sequence used refocusing B_0 gradient crusher pulses around the slice-selective 180° RF pulse, and also before and after the last 90° RF pulse. In order to improve the SNR from the localized volume, multiple averages could be used in combination with or without a multistep RF phase cycling to minimize any artifacts stemming from improper RF pulses. The 2D L-COSY sequence has been successfully implemented and evaluated on 7, 3, and 1.5 T MRI scanners manufactured by different vendors.[38–46]

To understand the nature of the interactions between spins during the evolution, mixing, and detection periods, and how these events modulate the amplitude, frequency, and phase of the 2D spectral signal array, a closer look at the time evolution of a weakly coupled AX type spin-pair system with two protons A and X, whose chemical shift is large compared to the J-coupling between them, is considered here. Using the density matrix formalism, the time course of evolution of coherences and magnetization is presented at the different time points marked in Figure 30.1 to describe the spin state before and after each RF pulse, as well as its evolution during different time intervals.

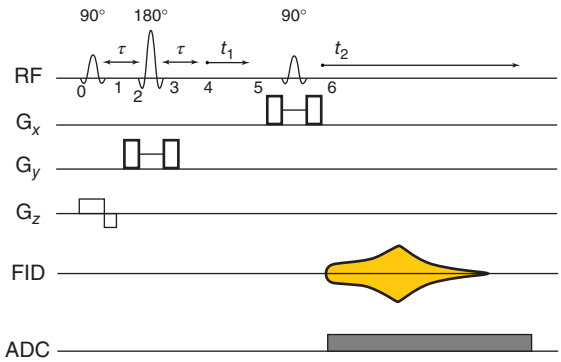

Figure 30.1. A schematic diagram of the 2D L-COSY sequence containing three slice-selective RF pulses (90°, 180°, 90°) for volume localization. The B_0-crusher gradient pulses were played around the 180° refocusing and the second 90° coherence transfer RF pulses. After the evolution during 2τ, there is a formation of the Hahn spin echo. Direct acquisition along t_2 and indirect detection along t_1 enable encoding of two spectral dimensions

The weakly coupled AX spin system has four energy levels that can lead to 4 observable single quantum (SQ) coherences (ω_{12}, ω_{34}, ω_{13}, ω_{24}) and nonobservable multiple quantum (zero and double quantum) coherences: ω_{23} and ω_{14} under different perturbations.[37,47] At time point 0 before the first slice-selective 90° RF pulse, the spins are at the Boltzmann equilibrium, and the spin state is described by the F_z matrix as shown below:

$$\rho_0 \propto \begin{pmatrix} 1 & 0 & 0 & 0 \\ 0 & 0 & 0 & 0 \\ 0 & 0 & 0 & 0 \\ 0 & 0 & 0 & -1 \end{pmatrix} \tag{30.1}$$

We assume that the RF pulses are applied along the y-direction in the rotating frame of reference so that the RF pulse rotation operators contain only real numbers. The spin state after the rotation by the first 90° RF pulse along the y-direction (time point 1) is the observable F_x matrix containing nonzero elements for the four SQ coherences:

$$\rho_1 \propto P_y^{-1} F_z P_y$$

$$\rho_1 \propto \frac{1}{4} \begin{pmatrix} 1 & -1 & -1 & 1 \\ 1 & 1 & -1 & -1 \\ 1 & -1 & 1 & -1 \\ 1 & 1 & 1 & 1 \end{pmatrix} \begin{pmatrix} 1 & 0 & 0 & 0 \\ 0 & 0 & 0 & 0 \\ 0 & 0 & 0 & 0 \\ 0 & 0 & 0 & -1 \end{pmatrix}$$

$$\begin{pmatrix} 1 & 1 & 1 & 1 \\ -1 & 1 & -1 & 1 \\ -1 & -1 & 1 & 1 \\ 1 & -1 & -1 & 1 \end{pmatrix} \propto \frac{1}{2}\begin{pmatrix} 0 & 1 & 1 & 0 \\ 1 & 0 & 0 & 1 \\ 1 & 0 & 0 & 1 \\ 0 & 1 & 1 & 0 \end{pmatrix} \quad (30.2)$$

After time point 2, the SQ coherences start evolving during τ as shown in Figure 30.1 and the density matrix is

$$\rho_2 \propto \begin{pmatrix} 0 & e^{-i\omega_{(12)}\tau} & e^{-i\omega_{(13)}\tau} & 0 \\ e^{i\omega_{(12)}\tau} & 0 & 0 & e^{-i\omega_{(24)}\tau} \\ e^{i\omega_{(13)}\tau} & 0 & 0 & e^{-i\omega_{(34)}\tau} \\ 0 & e^{i\omega_{(24)}\tau} & e^{i\omega_{(34)}\tau} & 0 \end{pmatrix} \quad (30.3)$$

The evolving SQ coherences are characterized by

$$\omega_{12} \propto (\delta_X + J/2),\ \ \omega_{34} \propto (\delta_X - J/2),$$
$$\omega_{13} \propto (\delta_A + J/2) \text{ and } \omega_{24} \propto (\delta_A - J/2) \quad (30.4)$$

where δ_A and δ_X are the chemical shifts of spins A and X and J represents the indirect spin–spin coupling (in rad s^{-1}) that is communicated through the covalent bonds. The direct spin–spin dipolar coupling between the A and X protons communicated through space is assumed to average to zero due to the tumbling motion of these spins. After the evolution through crusher gradient pairs and slice-selective refocusing of the 180° RF pulse at the end of τ, the spin state is described by

$$\rho_3 \propto {R_y}^{-1}\rho_2 R_y \propto \frac{1}{2}\begin{pmatrix} 0 & 0 & 0 & 1 \\ 0 & 0 & -1 & 0 \\ 0 & -1 & 0 & 0 \\ 1 & 0 & 0 & 0 \end{pmatrix} \begin{pmatrix} 0 & e^{-i\omega_{(12)}\tau} & e^{-i\omega_{(13)}\tau} & 0 \\ e^{i\omega_{(12)}\tau} & 0 & 0 & e^{-i\omega_{(24)}\tau} \\ e^{i\omega_{(13)}\tau} & 0 & 0 & e^{-i\omega_{(34)}\tau} \\ 0 & e^{i\omega_{(24)}\tau} & e^{i\omega_{(34)}\tau} & 0 \end{pmatrix} \begin{pmatrix} 0 & 0 & 0 & 1 \\ 0 & 0 & -1 & 0 \\ 0 & -1 & 0 & 0 \\ 1 & 0 & 0 & 0 \end{pmatrix} \propto \frac{1}{2}\begin{pmatrix} 0 & -e^{i\omega_{(34)}\tau} & -e^{i\omega_{(24)}\tau} & 0 \\ -e^{-i\omega_{(34)}\tau} & 0 & 0 & -e^{i\omega_{(13)}\tau} \\ -e^{-i\omega_{(24)}\tau} & 0 & 0 & -e^{i\omega_{(12)}\tau} \\ 0 & -e^{-i\omega_{(13)}\tau} & -e^{-i\omega_{(12)}\tau} & 0 \end{pmatrix} \quad (30.5)$$

Now, the SQ coherences included in equation (30.5) will evolve under another period, τ and at the end of this period, the first Hahn spin echo is described by

$$\rho_4 \propto -\frac{1}{2}\begin{pmatrix} 0 & e^{i(\omega_{(34)}-\omega_{(12)})\tau} & e^{i(\omega_{(24)}-\omega_{(13)})\tau} & 0 \\ e^{i(\omega_{(12)}-\omega_{(34)})\tau} & 0 & 0 & e^{i(\omega_{(13)}-\omega_{(24)})\tau} \\ e^{i(\omega_{(13)}-\omega_{(24)})\tau} & 0 & 0 & e^{i(\omega_{(12)}-\omega_{(34)})\tau} \\ 0 & e^{i(\omega_{(24)}-\omega_{(13)})\tau} & e^{i(\omega_{(34)}-\omega_{(12)})\tau} & 0 \end{pmatrix} \propto -\frac{1}{2}\begin{pmatrix} 0 & e^{-i2\pi J\tau} & e^{-i2\pi J\tau} & 0 \\ e^{i2\pi J\tau} & 0 & 0 & e^{i2\pi J\tau} \\ e^{i2\pi J\tau} & 0 & 0 & e^{i2\pi J\tau} \\ 0 & e^{-i2\pi J\tau} & e^{-i2\pi J\tau} & 0 \end{pmatrix} \quad (30.6)$$

It is evident from equation (30.6) that the chemical shift and any other linear interaction terms are refocused at the time of the Hahn spin echo and that the spin state contains phase terms with only the bilinear J-coupling term. The rotation operators P_y and R_y used in equations (30.2) and (30.5) represent the 90° and 180° RF pulses, respectively.[47]

The spin state ρ_4 is followed by encoding of the second spectral dimension with a variable time period t_1, meaning that during a series of repeat experiments, t_1 takes on a different set of values that is similar to phase encoding a second spatial dimension in MRI. The evolution time (t_1) is being incremented here, as opposed to incrementing the amplitude of the phase-encoding gradient in conventional MRI.

$$\rho_5 \propto -\frac{1}{2}\begin{pmatrix} 0 & Ke^{-i\omega_{(12)}t_1} & Ke^{-i\omega_{(13)}t_1} & 0 \\ K^*e^{i\omega_{(12)}t_1} & 0 & 0 & K^*e^{-i\omega_{(24)}t_1} \\ K^*e^{i\omega_{(13)}t_1} & 0 & 0 & K^*e^{-i\omega_{(34)}t_1} \\ 0 & Ke^{i\omega_{(24)}t_1} & Ke^{i\omega_{(34)}t_1} & 0 \end{pmatrix} \quad (30.7)$$

where $K = e^{-i2\pi J\tau}$ and $K^* = e^{i2\pi J\tau}$.

After the evolution during t_1, the spins evolve during a mixing period in which a slice-selective 90° RF pulse is applied in the third orthogonal plane, again sandwiched by gradient crusher pulses:

$$\rho_6 \propto {P_y}^{-1}\rho_4 P_y \propto -\frac{1}{8}\begin{pmatrix} 1 & -1 & -1 & 1 \\ 1 & 1 & -1 & -1 \\ 1 & -1 & 1 & -1 \\ 1 & 1 & 1 & 1 \end{pmatrix} \begin{pmatrix} 0 & Ke^{-i\omega_{(12)}t_1} & Ke^{-i\omega_{(13)}t_1} & 0 \\ K^*e^{i\omega_{(12)}t_1} & 0 & 0 & K^*e^{-i\omega_{(24)}t_1} \\ K^*e^{i\omega_{(13)}t_1} & 0 & 0 & K^*e^{-i\omega_{(34)}t_1} \\ 0 & Ke^{i\omega_{(24)}t_1} & Ke^{i\omega_{(34)}t_1} & 0 \end{pmatrix}$$

$$\begin{pmatrix} 1 & 1 & 1 & 1 \\ -1 & 1 & -1 & 1 \\ -1 & -1 & 1 & 1 \\ 1 & -1 & -1 & 1 \end{pmatrix} \tag{30.8}$$

Only the SQ elements of ρ_6 are observable. These are

$$(\rho_6)_{12} \propto -1/8\{-K^*(e^{i\omega 12t1} + e^{i\omega 13t1} - e^{-i\omega 24t1} - e^{-i\omega 34t1}) + K(e^{-i\omega 12t1} - e^{-i\omega 13t1} + e^{i\omega 24t1} - e^{i\omega 34t1}) \tag{30.9}$$

$$(\rho_6)_{34} \propto -1/8\{-K^*(e^{i\omega 12t1} - e^{i\omega 13t1} + e^{-i\omega 24t1} - e^{-i\omega 34t1}) + K(e^{-i\omega 12t1} + e^{-i\omega 13t1} - e^{i\omega 24t1} - e^{i\omega 34t1}) \tag{30.10}$$

$$(\rho_6)_{13} \propto -1/8\{-K^*(e^{i\omega 12t1} + e^{i\omega 13t1} - e^{-i\omega 24t1} - e^{-i\omega 34t1}) - K(e^{-i\omega 12t1} - e^{-i\omega 13t1} + e^{i\omega 24t1} - e^{i\omega 34t1}) \tag{30.11}$$

$$(\rho_6)_{24} \propto -1/8\{K^*(e^{i\omega 12t1} - e^{i\omega 13t1} + e^{-i\omega 24t1} - e^{-i\omega 34t1}) + K(e^{-i\omega 12t1} + e^{-i\omega 13t1} - e^{i\omega 24t1} - e^{i\omega 34t1}) \tag{30.12}$$

Similarly, the lower diagonal elements $[(\rho_6)_{21}, (\rho_6)_{43}, (\rho_6)_{31}$, and $(\rho_6)_{42}]$ will also have observable SQ coherences. After this, the data acquisition or detection period, t_2 begins in the L-COSY experiment, during which the digitized signal is recorded as a function of t_2 (direct), similar to conventional 1D MRS. This is repeated several times creating a 2D data matrix in which each row represents a different t_1 (indirect) modulation. The 2D signal acquired by the analog-to-digital converter (ADC) is given by

$$\mathbf{s}(t_1, t_2) = \mathrm{Tr}[(F_x)\rho_5] \exp(-i\omega_2 t_2) \exp(-t_1/T_2) \exp(-t_2/T_2) [1 - \exp(-\mathrm{TR}/T_1)] \tag{30.13}$$

where 'Tr' in the equation (30.13) means the sum over all diagonal elements.

From equations (30.9) through (30.13), it is clear that there is a coherence transfer between A and X, which are J-coupled spins. A 2D Fourier transform (FT) along both the t_1 and t_2 axes will result in a 2D MR spectrum as a function of the two frequency variables (F_1, F_2) described by

$$\mathbf{S}(F_1, F_2) = \iint \mathbf{s}(t_1, t_2)\, dt_1 dt_2 \tag{30.14}$$

The signal acquisition array, $\mathbf{s}(t_2, t_1)$, is the basis of 2D spectroscopy and as discussed in the latter sections of this chapter, the signal acquisition can be extended to further spatial dimensions by adding 2 or 3 spatially encoding gradients to the sequence, thereby enabling multivoxel 2D MRS in a single slice or a three-dimensional (3D) volume.

As discussed by Aue *et al*.,[37] the diagonal peaks and cross-peaks can be dispersive and absorptive, respectively, when two hard 90° RF pulses are used to acquire the COSY spectrum. Mixed line shapes in the 2D NMR spectra are typically due to eddy currents (ECs) from the spatial-encoding gradient pulses. Both the diagonal peaks and cross-peaks of an L-COSY spectrum have mixed phases along the F_1 axis, as reported earlier.[38–40] In contrast to the amplitude modulation in conventional COSY,[37] the phase modulation in L-COSY is caused by the evolution of the signal during the gradient pulse before the last 90° RF pulse.[38–40] A pure-phase L-COSY spectrum can be recorded using a quadrature detection method along the F_1 axis, as described by Brereton *et al*.[48] This requires two separate *P*- and *N*-type spectral acquisitions and recombination of the two datasets, where *N* and *P* represent a 'coherence transfer echo' and a 'coherence transfer antiecho', respectively, selected using different polarities of gradient pulses.[48–51] As discussed by Keeler,[51] the *N* stands for 'negative', which is due to the coherence order during t_1 being of opposite sign to that along t_2. In contrast, *P* stands for 'positive' due to the same sign of the coherences during the two spectral dimensions, t_1 and t_2.

30.2.2 Apodization Filters for 2D L-COSY

The 2D L-COSY spectrum will contain peaks along the diagonal that are similar to those of 1D MRS and cross-peaks connecting multiplets of spins that are J-coupled.[37,38] The diagonal-peak intensities follow a cosine dependence, and time-domain cross-peak amplitudes increase from zero at the beginning to a maximum at 1/2 J, with the signal decaying according to the inhomogeneously broadened T_2s (T_2*). Hence, it is advisable to weight the time-domain signal by a weighting function that de-emphasizes the signal for small t_2 and t_1 values.[49–51]

As shown in Figure 30.2, optimal matching filters such as a sine-bell (SB) or skewed squared SB can be used along both dimensions for better sensitivity of cross-peaks in the 2D L-COSY spectrum. Use of

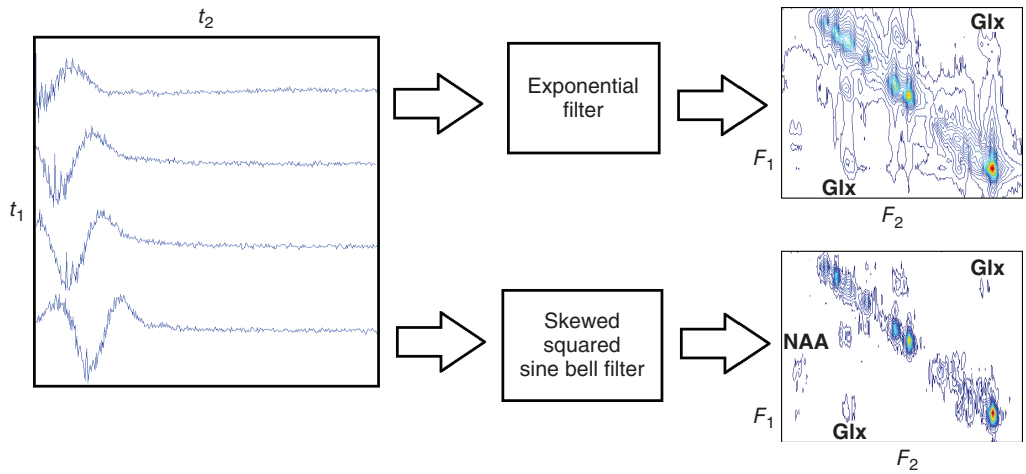

Figure 30.2. Comparison of exponential and sine-bell filters for processing the 2D L-COSY sequence; even though the raw data matrix (t_2, t_1) contained 100 t_1 signals, only 4 t_1 signals are shown on the left

the skewed squared SB filter instead of a conventional exponential filter for processing the 2D spectrum in Figure 30.2 has three major advantages.[52] First, unlike the exponential filter, the SB filter begins with a zero value and can emphasize cross-peaks relative to 2D diagonal peaks that are cosine dependent. Second, the SB filter removes broad wings (dispersive components) from 2D magnitude line shapes. Third, truncation errors due to apodization are minimized at the end of the time domain: because of the trailing edge of the SB function, the window function goes smoothly to zero.

30.2.3 Eddy Current (EC) Correction

As shown in Figure 30.1, the 2D L-COSY sequence uses three slice-selective RF pulses combined with spatial gradient pulses. The intense crusher gradient pulses at each side of the second and third RF pulses are used to minimize unwanted coherences arising from imperfect RF pulse refocusing and coherence transfer.[50,51] As with 1D MRS, 2D MRS is also sensitive to time-dependent frequency shifts that typically last a few milliseconds and that are induced by ECs due to switching the gradients on and off. These affect the first few points of the detected signal array along the t_2 dimension. ECs produce time-dependent magnetic fields that add to the gradient fields and contribute an EC-related phase to each t_2 signal. In order to calculate an EC-free spectral signal, the phase calculated from an on-resonance signal can be subtracted from the EC-corrupted signal.[53–55] This requires acquisition of two independent L-COSY data matrices[55]: one with water-suppressed (WS) and one without nonwater-suppressed (NWS) water suppression, as depicted in the processing algorithm shown in Figure 30.3.[53–55] Even though multiple signals can be averaged for the WS data, one average typically suffices for the acquisition of the high SNR, NWS data.

Figure 30.4 shows 2D L-COSY spectra acquired from a 27 ml voxel in a phantom containing 21 brain metabolites at physiological concentrations acquired at 3 T, in about 30 min. The WS and NWS time-domain data were processed using the steps shown in Figure 30.3. The EC-uncorrected and corrected L-COSY (WS) data were postprocessed with (i) apodization using shifted squared SB filters applied in both frequency dimensions; (ii) zero filling once or twice along the t_2 and t_1 dimensions; and (iii) a complex fast FT (FFT) along two dimensions. Even though a classical *N*-type COSY spectrum is presented with the diagonal running from the lower left to upper right corner of the 2D spectral display, owing to the severe asymmetry of cross-peaks in vivo,[56] our practice is to present the 2D L-COSY spectrum with the diagonal running from the upper left to lower right corner.

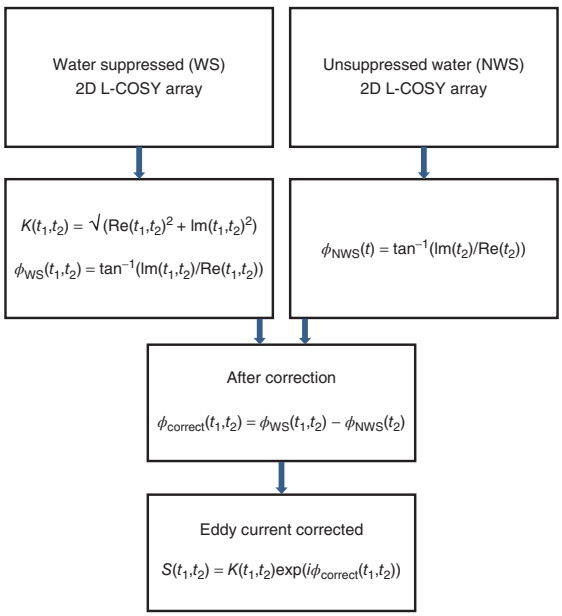

Figure 30.3. Eddy current (EC) correction scheme. Re and Im represent the real and imaginary parts of the complex time-domain signal; ϕ_{WS} and ϕ_{NWS} represent the phase angles calculated from the water-suppressed and water-unsuppressed data sets

Figure 30.4(a) shows the 2D L-COSY spectrum without using the NWS data for EC correction. Using only the first signal ($\Delta t_1 = 0$) from the NWS array for EC correction results in the L-COSY spectrum shown in Figure 30.4(b). Figure 30.4(c) shows the L-COSY spectrum after the EC correction of the WS array using all rows of the NWS array. However, the improvement observed in the phantom following EC correction was minimal in this case, possibly due to less impact of EC on coherence transfer echoes in the 2D L-COSY data. The more significant impact of EC on a multivoxel-based correlated spectroscopic imaging data will be discussed in a latter section.

30.2.4 Localized Spin-echo Correlated Spectroscopy (L-SECSY)

Even though there is no real limitation on the number of complex points along the detected t_2 dimension, the resolution along the F_1 dimension of COSY is dictated by the total number of t_1 increments, which directly affects the acquisition duration. Nagayama *et al*. proposed a novel sequence called *spin-echo correlated spectroscopy* (*SECSY*) in which the incremental delay was equally added before and after the coherence transfer 90° RF pulse. This reduced the number of t_1 increments and spectral width along the F_1 dimension.[57] Following the same strategy, we presented a second variation of L-COSY, namely localized spin-echo correlation spectroscopy (L-SECSY).[58] Localized SECSY works the same way as L-COSY (Figure 30.1), except that the second incremental period (Δt_1) after the coherence transfer 90° RF pulse is set the same as the first t_1 evolution period. Compared to L-COSY, the diagonal peaks of L-SECSY lie on ($F_1 = 0$) and the *J*-cross-peaks are symmetrically disposed above and below the diagonal, falling on a straight line intersecting the diagonal at 45°. The application of 2D L-SECSY was demonstrated in a brain phantom and in healthy human brain at 1.5 T.[58] Inclusion of t_1 encoding before and after the last 90° RF pulse leads to severe T_2* weighting. One solution that minimizes this loss is to acquire the data with the t_1 increments before the 90° RF pulse only (similar to 2D L-COSY) and then impose the phase shift for the second t_1 evolution as shown in Figure 30.5. The phase shift is required along the t_1 dimension only, so the 2D array must be Fourier transformed once along the t_2 dimension and the t_1 signals multiplied by a phase factor of exp ($-2\pi F_2 t_1$).

Shown in Figure 30.6 are (i) a voxel location on an axial MRI and (ii) the corresponding 2D L-COSY spectrum acquired from a 35-year-old healthy human subject. The 2D L-COSY data were acquired using the same acquisition parameters that were used for the brain phantom in Figure 30.4, and the WS L-COSY array was phase-corrected using the EC correction scheme in Figure 30.3, based on the first row of the NWS data. The 2D L-COSY data shown in Figure 30.6(b) were phase rotated as discussed above (Figure 30.5). Figure 30.6(c) is the resulting 2D L-SECSY spectrum after phase rotation. An advantage of L-SECSY over L-COSY is that a smaller sweep width (1250 Hz vs ±312.5 Hz) is needed along F_1.

30.2.5 2D *J*-resolved Spectroscopy Using PRESS (JPRESS)

Another 2D technique that can be used for improved peak dispersion in the spectral domain is the *J*-resolved spectroscopy (JPRESS) sequence. This method was initially proposed for high-resolution NMR

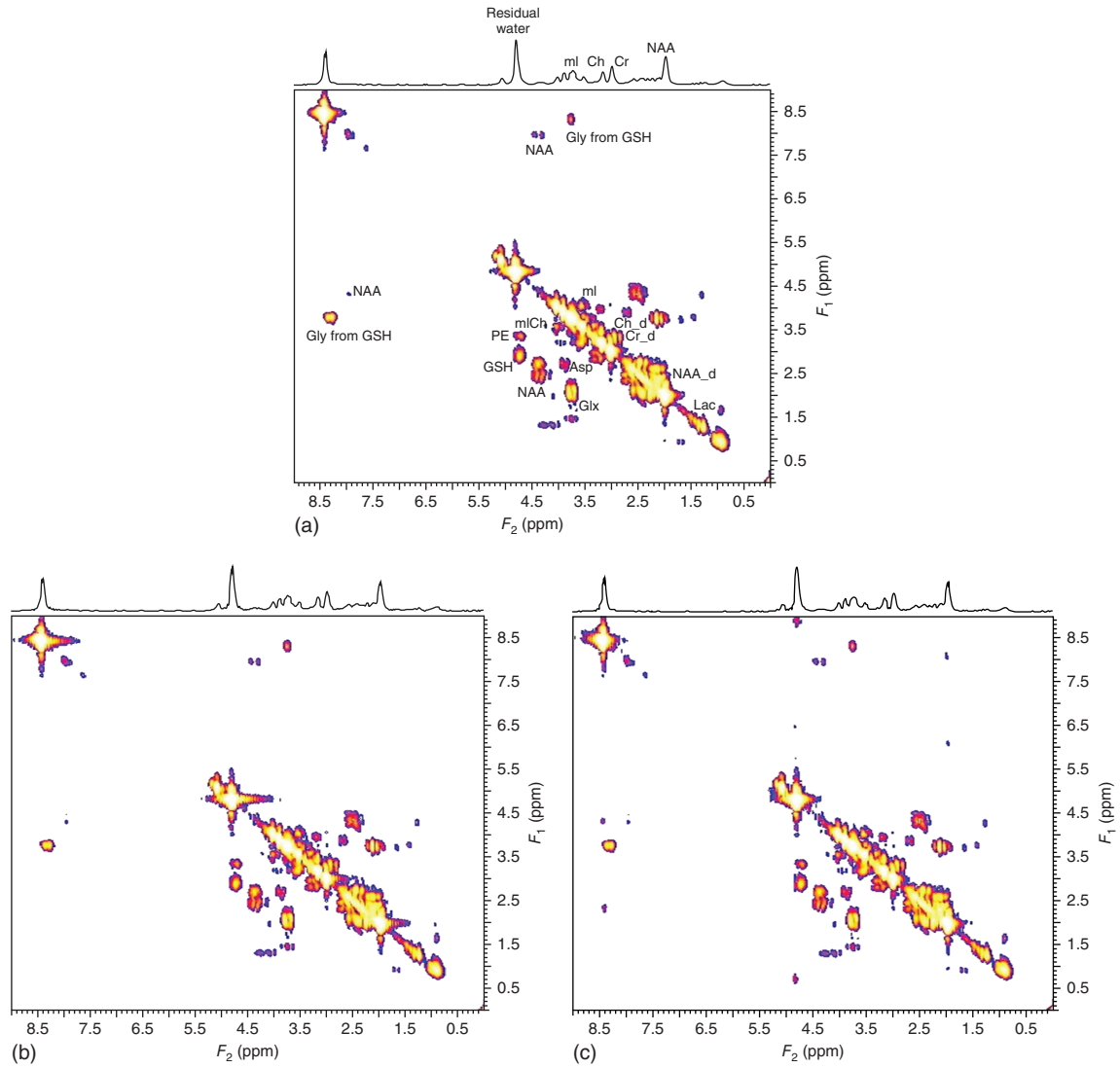

Figure 30.4. 2D L-COSY spectra acquired at 3 T from a 27 ml voxel in a phantom comprised of brain metabolites at physiological concentrations. (a) The EC-uncorrected spectrum with water suppression (WS) only. (b) EC corrected with WS using the first row of the non-water-suppressed (NWS) spectrum only. (c) EC corrected with WS using all rows of the NWS data. The phantom comprised: 8.9 mM NAA, 0.7 mM GABA, 2.1 mM aspartate (Asp), 0.9 mM choline (Ch), 7 mM creatine (Cr), 1 mM glucose (Glc), 12.5 mM glutamate (Glu), 2.5 mM glutamine (Gln), 10 mM glutathione (GSH), 4.4 mM myo-inositol (mI), 1.0 mM lactate (Lac), 0.6 mM phosphocholine (PCh), 1.8 mM taurine (Tau), 1.0 mM threonine (Thr), 1 mM phosphoethanolamine (PE), 1 mM lysine (Lys), 1 mM valine (Val), 1 mM leucine (Leu), 1 mM isoleucine (iLeu), 1 mM alanine (Ala), 100 mM formate, 5 mM sodium azide, and 1 mM dimethyl sulfoxide (DSS) in a phosphate buffer solution to maintain pH at 7.2. Acquisition parameters were echo time, TE = 30 ms; sequence repetition time, TR = 2 s; total number of scans = 800; and 100 Δt_1 increments with eight averages/Δt_1 for WS and one average/Δt_1 for NWS. Total scan times were 26 min (WS) and 3 min (NWS)

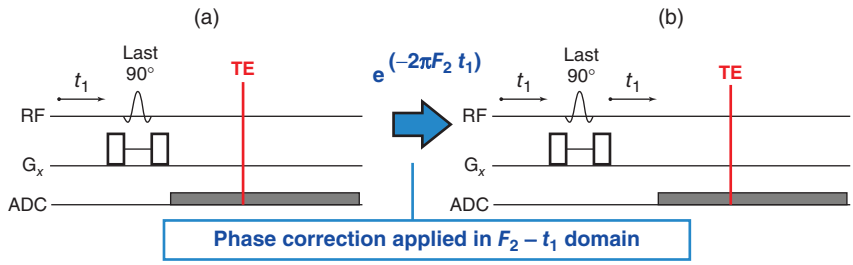

Figure 30.5. (a) Partial 2D L-COSY sequence showing the t_1 increments and 90° RF pulse followed by detection along t_2. (b) Conversion of the 2D L-COSY sequence into a 2D L-SECSY is depicted

spectroscopy[49–51], but has been successfully adapted for in vivo MRS[31,32,40,59,60] using the PRESS sequence for spatial localization. Accordingly, the new 2D sequence is named 'JPRESS'.[32] Chemical shift information in addition to that of the J-coupling is acquired along the t_2 (detected/direct) dimension, whereas the t_1 (indirect) dimension only contains J-coupling information. Originally, the in vivo JPRESS sequence was developed by adding the t_1 increment before and after the last 180° pulse. Subsequently, the direct dimension was acquired with a half-echo sampling scheme as shown in Figure 30.7(a).[31,32,40,59,60]

A more efficient way to perform the JPRESS experiment was demonstrated by Schulte *et al*., also depicted in Figure 30.7.[34,61,62] This modified JPRESS has two major differences from the earlier version: (i) the t_1 increment is only before the last 180° pulse and (ii) the data acquisition starts immediately after the crusher gradient pulse next to the last 180° RF pulse. This is called *a maximum-echo sampling* scheme (Figure 30.7a). Half-echo sampling starts data acquisition at the echo time (TE), whereas maximum-echo sampling starts collecting data after the last crusher gradient is played out. Maximum-echo sampling has been shown to improve sensitivity compared with the half-echo sampling scheme for JPRESS.[34,60,61]

As in the reconstruction of L-SECSY from the L-COSY data, a linear phase correction must be applied to the data along the F_2–t_1 dimension when using the maximum-echo sampling scheme[34]:

$$\text{Phase correction}\,(F_2, t_1)\ \text{factor} = \exp(-2\pi F_2 t_1) \tag{30.15}$$

where $t_1 = \text{TE} - \text{TE}_{\text{min}}$ and F_2 is the frequency along the direct dimension. This linear phase correction is necessary because each echo needs to be shifted to the same temporal point and is equivalent to adding a second t_1 increment after the last 180° pulse. However, B_0 inhomogeneity is not refocused using this postprocessing method. A schematic of the linear phase corrections is shown in Figure 30.7(b).

The phase corrections have implications for the spectral bandwidth along the indirect dimension (BW_1). For example, suppose $\Delta t_1 = 1$ ms, so that $\text{BW}_1 = 1000$ Hz (± 500 Hz). After the linear phase correction is applied by adding a second t_1 increment, $\Delta t_1 = 2$ ms and BW_1 is now only ± 250 Hz. This is important to note when designing the maximum-echo sampling experiment. JPRESS has been used for in vivo studies of the human brain,[31,32,40,59] muscle,[33] prostate,[60,63] and breast.[64] Quantitation methods incorporating prior knowledge exist to help fit metabolite peaks that are difficult to identify with traditional 1D (chemical shift) spectroscopy.[34,36,43] This makes JPRESS a powerful 2D technique for the investigation of different metabolites in vivo.

30.2.6 Apodization Filters for 2D JPRESS

The J-coupled multiplets are better resolved along the indirect t_1 dimension than in the detected t_2 (direct) dimension, as any defocusing linear B_0 interactions including the static field inhomogeneity during the first half of t_1 are refocused during the second half, resulting in a net zero dependence on the B_0 inhomogeneity and other static field interactions. Even though this is a major advantage, the phase-modulated time-domain datasets are transformed into phase-twisted 2D peaks after the double FFT of the 2D JPRESS raw data. Hence, the squared or simple SB filter functions described in Section 30.2.2 can be used before the double FFT.

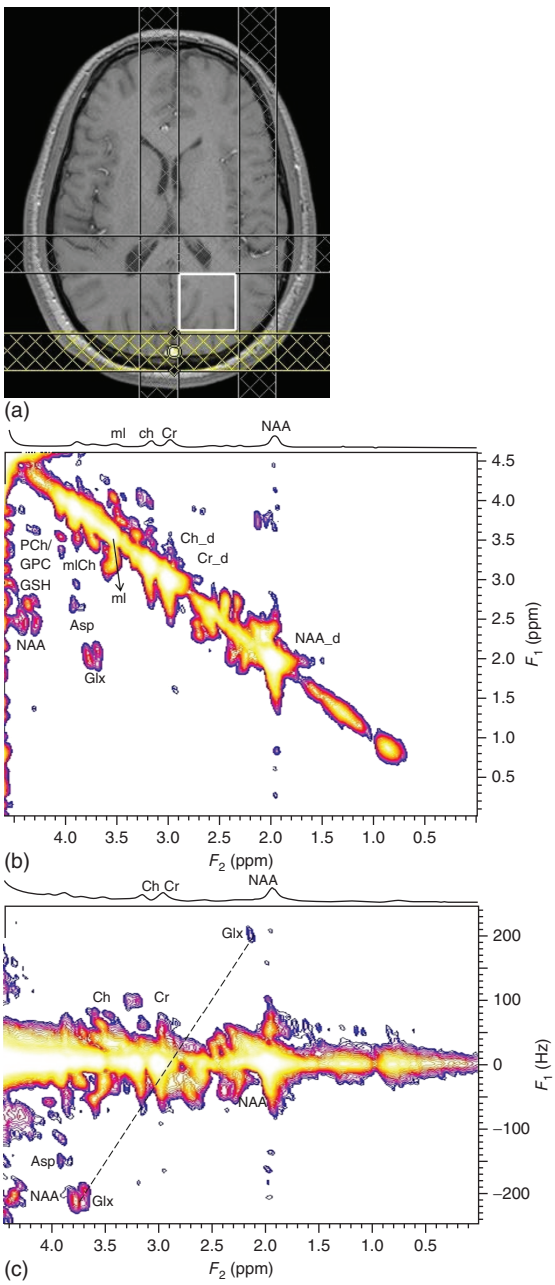

Figure 30.6. 2D L-COSY spectrum acquired from a 35-year-old healthy human subject: (a) Axial MRI slice showing the voxel location. (b) Water-suppressed (WS) L-2D COSY spectrum using only the first row of the non-WS (NWS) data for EC correction. (c) Conversion of the 2D L-COSY data from (b) into 2D L-SECSY, after phase rotating the data (Figure 30.3)

30.2.7 Strong Coupling Effects in 2D JPRESS

One of the advantages of JPRESS over L-COSY is that the chemical shift and any linear interaction are refocused during the t_1 dimension while the J-interaction remains unrefocused. At 3 T or lower B_0, this assumption is applicable only for weakly coupled metabolites such as lactate, alanine, and glycine. Most other metabolites have strongly coupled protons where J-coupling is equal to or larger than their chemical shifts ($\delta < J$). Hence, the refocusing 180° RF pulse at the center of the t_1 evolution does not refocus all chemical shifts and results in more cross-peaks. It has been demonstrated earlier that 2D JPRESS spectra of brain and prostate metabolites contain more cross-peaks than those of weakly coupled ones.[32,60]

30.2.8 Adiabatic COSY and JPRESS

One of the limitations of in vivo MRS/MRSI using conventional RF pulses performed at 3 T or higher fields is the chemical shift displacement error (CSDE),[65–67] defined as the difference in the location of the center of the excitation or refocusing slices of two resonances with a different chemical shift (see Chapter 7). With NMR signal excitation using large body coils, the bandwidths of conventional refocusing RF pulses, such as optimized 180° pulses,[68] become quite small. As the chemical shift increases with B_0, the CSDE at 3 T and higher fields can become very large, if ignored.

A second problem with MRS/MRSI using conventional RF pulses is the difficulty of achieving a uniform RF transmit (B_1) field, leading to poor slice-selection profiles. Accurate volume selection using slice-selective RF pulses is a prerequisite for proton (^{1}H) MRSI of the brain in order to exclude contamination by large lipid signals from the skull and/or water signals from poorly shimmed regions outside the selected volume. Owing to inhomogeneous transmit B_1 fields, flip angles may vary inside the voxel, causing not only signal loss but also an increase in the side lobes of the slice profile, leading to nonzero flip angles outside the selected volume.[69,70] In addition, when strongly coupled spin systems are observed in spin-echo experiments, the spectral shape of the corresponding signals can vary, depending on the local flip angle of the refocusing pulses.[71] PRESS-localized MRSI also has the complication of unreliable spectra at the edges of the PRESS box due

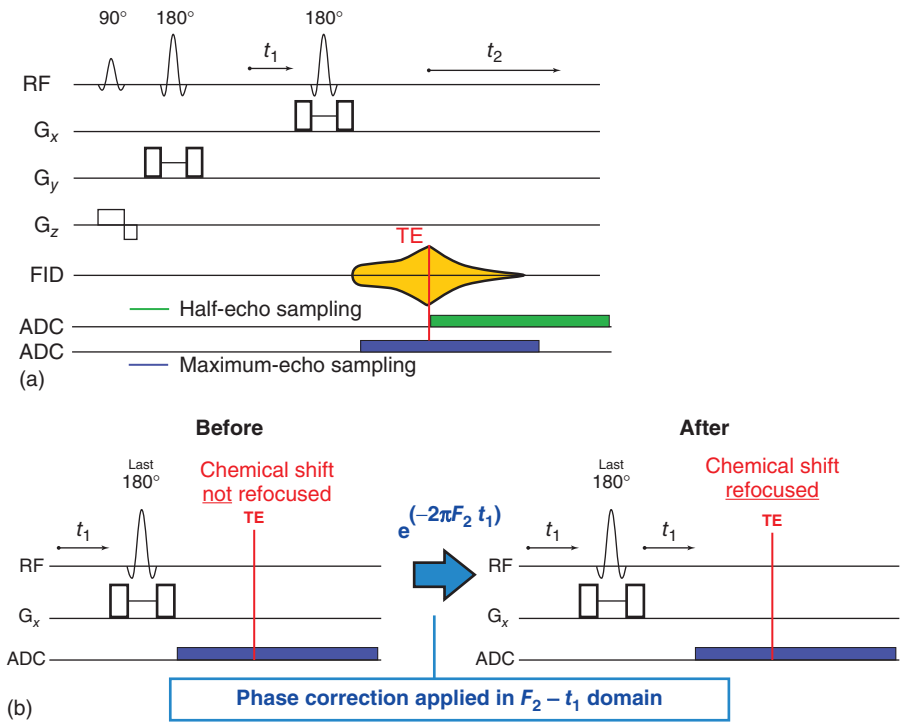

Figure 30.7. (a) A schematic for a JPRESS sequence utilizing maximum-echo sampling for acquisition (highlighted in gold; FID; ADC, analog-to-digital converter). Half-echo sampling is started exactly at the echo time (green), whereas maximum-echo sampling starts immediately after the last crusher gradient (blue). The number of t_2 points sampled using each method is the same. (b) The effects of adding a linear phase correction to refocus the chemical shift information. The linear phase acts as if a second t_1 increment is added after the last 180° pulse. The linear phase correction effectively halves the spectral bandwidth in the indirect dimension

to the imperfect slice profiles of the 180° pulses. All of these limitations and potential artifacts apply equally to L-COSY and JPRESS. In addition, the efficiency of coherence transfer echoes may suffer when the 90° RF pulses are inhomogeneous, resulting in suboptimal cross-peaks in L-COSY.

These shortcomings can be addressed using adiabatic pulses, as they have relatively high bandwidths, and their flip angles are insensitive to transmit B_1 inhomogeneities, as demonstrated by Garwood and DelaBarre.[65] Adiabatic-refocusing pulses have sharp slice-selection profiles to produce a localized Hahn spin echo. The adiabatic excitation or refocusing pulses have been implemented in techniques such as 'LASER' (localization by adiabatic selective refocusing)[66,72] and its simplified version semi-localization by adiabatic selective refocusing (sLASER; see Chapter 7).[66,67] The sLASER sequence consists of a conventional nonadiabatic 90° slice-selective pulse and two pairs of adiabatic hyperbolic secant (HS) pulses for refocusing. While some insensitivity to B_1 inhomogeneity is lost, the sLASER sequence has reduced RF power and can achieve shorter TEs than LASER. For pulse spacing that is short compared to the reciprocal of the J-coupling and the chemical shift bandwidth, J-coupling losses will generally be minimal despite short echo times and can be neglected.[73] The two adiabatic RF-refocusing pulse pairs can reduce antiphase coherence that results from J-coupling and has been shown to improve the spectral shape of coupled spin systems at 3 T.[67] With the small CSDE and sharp-selection profiles of the adiabatic-refocusing pulses, the VOI can be positioned close to the skull, while largely avoiding contamination from subcutaneous lipid signals from outside the voxel.

Ramadan *et al*. implemented an adiabatic localized correlated spectroscopy (AL-COSY) in which the

VOI was localized by a 90° nonselective adiabatic RF pulse for excitation followed by two pairs of adiabatic HS RF pulses for refocusing and a terminal 90° RF sine pulse for the coherence transfer.[74] Compared to L-COSY using nonadiabatic 90° and modified Mao[74] 180° RF pulses, chemical shift artifacts were reduced with AL-COSY and slice profiles of adiabatic pulses were found to be sharper and more symmetrical than those obtained with conventional Mao pulses.[68]

Another adiabatic version of L-COSY was proposed by Lin *et al*.[75] They showed that an 'sLASER-first-COSY' sequence yielded stronger cross-peaks and higher ratios of cross-peak volumes to diagonal-peak volumes than the 'sLASER-last-COSY' sequence in which the nonselective hard 90° coherence transfer RF pulse is replaced by a slice-selective 90° RF pulse. In addition, these authors presented two adiabatic versions of JPRESS: the first used three pairs of adiabatic pulses for voxel localization for *J*-resolved LASER and the second used two pairs of 180° RF pulses in sLASER.[76] The first half of the t_1 period was inserted between the last pair of adiabatic pulses, to record 2D *J*-resolved spectra in phantoms and human brain. Significant advantages over conventional JPRESS were demonstrated. These were that: (i) the *J*-resolved LASER and sLASER sequences exhibited better suppression of both chemical shift artifacts and additional *J*-refocused peaks that arise from spatially dependent J-coupling evolution; and (ii) they were relatively insensitive to RF frequency offset over a large bandwidth. However, there were also a few drawbacks: the adiabatic versions had higher RF power specific absorption rates (SARs) and slightly longer TE compared to the basic versions of L-COSY and JPRESS.

30.3 ECHO-PLANAR CORRELATED AND *J*-RESOLVED MRSI

30.3.1 MRSI/Echo-planar Spectroscopic Imaging

Depending on the desired spatial resolution, traditional 2D or 3D MRSI[25–27] with conventional CSI phase-encoding schemes generally lead to intolerable scan times. To sample a 3D volume with numbers of phase-encoding steps N_x, N_y, and N_z along all three spatial dimensions (x, y, z), with a repetition time TR, and number of averages per frame of N_{AV}, requires a total measurement time of $N_x \times N_y \times N_z \times \mathrm{TR} \times N_{AV}$. Thus, for a simple 3D CSI acquisition with an N_{AV} of 1, a spatial matrix size of $16 \times 16 \times 8$, and TR = 2 s, the total scan time will be more than an hour. Although all of the gradient phase-encoding steps contribute to the SNR, if the MRSI scan requires multiple averages to achieve adequate SNR, or longer TRs to avoid saturation effects, the resultant total acquisition time can easily render clinical applications impractical. In such scenarios, integrating multivoxel spatial-encoding techniques with multidimensional sequences, such as L-COSY and JPRESS that require extra spectral dimensions, results in MRSI sequences that are even less clinically feasible. Hence, novel MRSI techniques with reduced scan times are essential for implementing 2D and 3D spectroscopy in the clinic.

Different methods of performing MRSI that avoid discrete phase-encoding gradients in one or more dimension have been developed and implemented to address this time constraint. In 1983, Mansfield[77,78] proposed the use of an echo-planar readout gradient to simultaneously acquire one spatial and one spectral (temporal) dimensions during a single readout. That approach had the potential to greatly shorten the acquisition of 2D and 3D MRSI data, but owing to implementation issues with the gradients[79] at that time, it took an extra decade until 1994 when Posse *et al*.[80,81] implemented the first clinically applicable proton echo-planar spectroscopic imaging (PEPSI) protocol, also known as echo-planar spectroscopic imaging (EPSI)[81] (see also Chapter 12). In EPSI, a time-varying readout gradient is employed to frequency encode the same line in *k*-space repeatedly, so that the spatial information is collected as a function of time. In this way, phase encoding of that spatial dimension is not needed. The remaining spatial dimensions are phase-encoded sequentially, similar to spin-echo MRI, resulting in an acceleration of N_x times if the frequency encoding is performed along the x-direction, say. Such an acceleration by over an order-of-magnitude in total scan time makes it feasible to acquire spatially resolved multidimensional MRS data in a clinical setting,[82] collect 3D data sets,[82] or increase spatial resolution.

Four-dimensional (4D) echo-planar correlated spectroscopic imaging (EP-COSI) and echo-planar *J*-resolved spectroscopic imaging (EP-JRESI)[83–85] sequences combine the speed advantage of the EPSI readout with the increased spectral dispersion offered by 2D L-COSY/JPRESS, enabling collection of better-resolved 2D spectra from multiple regions. The EPSI readout acquires one spatial (k_x) dimension and

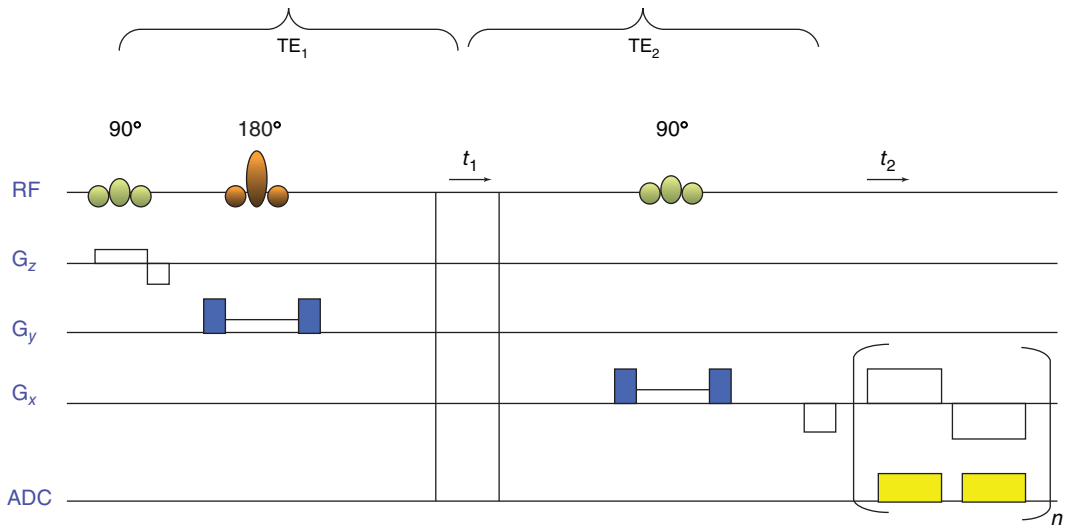

Figure 30.8. A schematic diagram of a 4D EP-COSI sequence

one temporal (t_2) dimension simultaneously, leaving the remaining spatial and spectral dimensions (k_y and t_1, respectively) to be recorded incrementally. This can reduce total scan time to around 20 min. In contrast, if one were to use conventional phase-encoding gradients (16×16) in combination with an L-COSY or JPRESS ($2048\,t_2$ and $100\,t_1$) sequence, the total acquisition time with TR of 2 s will be longer than 14 h.

30.3.2 4D Echo-planar Correlated Spectroscopic Imaging (EP-COSI)

A 4D EP-COSI sequence is shown in Figure 30.8, using two spatial encodings (k_x and k_y) and two spectral dimensions (t_2 and t_1). The sequence uses a 90°–180°–90° scheme for localizing the VOI with crusher gradients surrounding the refocusing 180° and coherence transfer 90° RF pulses. The crusher gradients ensure that magnetization outside of the VOI is dephased and does not significantly contribute to the acquired signal. The 'n' subscript along the ADC and G_x axes in Figure 30.8 represents the total number of echo-planar readout pairs (positive and negative) that result in the desired number of t_2 spectral points. TE_1 and TE_2 are the echo times for the first and the second echoes and $TE = TE_1 + TE_2$. As already noted, by utilizing the EPSI readout to acquire the k_x and t_2 data simultaneously, the total duration of the EP-COSI scan time is reduced N_x-fold. The second spatial dimension (k_y) is encoded using phase encoding, and the indirect temporal dimension (t_1) is acquired by incrementing the evolution time between the 180° and final 90° RF pulses by Δt_1. Some typical parameters for a 4D-EP-COSI experiment on a 3 T scanner include $k_x = 32$ (with oversampling), $k_y = 16$, t_2 points = 256, $\Delta t_2 = 0.84$ ms, t_1 points = 64, $\Delta t_1 = 0.8$ ms, TE = 30 ms, and TR = 1500 ms.

30.3.3 Echo-planar *J*-resolved Spectroscopic Imaging (EP-JRESI)

Replacing the second 90° slice-selective RF pulse in Figure 30.8. with a slice-selective 180° yields the 4D EP-JRESI sequence. As this sequence uses an EPSI readout as well, the acceleration factor remains N_x times a conventional 3D CSI. This sequence has the same advantages that JPRESS has over 2D L-COSY, mainly due to improved sensitivity as a result of refocusing the spin echo. Similar to 4D EP-COSI, the typical parameters for a 4D EP-JRESI experiment on a 3 T scanner include $k_x = 32$ (with oversampling), $k_y = 16$, t_2 points = 256, $\Delta t_2 = 0.84$ ms, t_1 points = 64, $\Delta t_1 = 1$ ms, TE = 30 ms, and TR = 1500 ms. The main difference between the two sequence parameters is that a spectral bandwidth of 1000 Hz is used for the indirect dimension in EP-JRESI, whereas EP-COSI

uses a spectral bandwidth of 1250 Hz for the indirect dimension. Of course, after phase corrections to account for the maximum-echo sampling scheme as described above, each 2D *J*-resolved spectrum that is extracted from the 4D EP-JRESI data will have a spectral bandwidth of ±250 Hz along the indirect spectral dimension (t_1), as discussed in Section 30.2.5. On the basis of the organ (prostate, brain, etc.) under investigation, scan parameters typically including the t_1 points, TE, and TR may need to be adjusted.

30.3.4 Postprocessing of the 4D EP-COSI/EP-JRESI Data

Reconstruction of 4D EP-COSI and EP-JRESI data sets is performed offline using custom MATLAB software macroroutines. Details for the reconstruction are provided in Figure 30.9. The center of the *k*-space is traversed repeatedly with a constant time interval in an ideal EPSI readout. Alternating readout gradients result in opposing directions for the trajectories along k_x. Hence, the odd/even echoes must be temporally reversed and the reversal of odd echoes translates this temporal shift in the echo train into a relative misalignment along k_x between the odd and even echoes. This misalignment generates spectral ghost artifacts when the echoes are combined. Echo misalignment due to the sample itself may be due to background gradients resulting from improper shimming, local susceptibility-induced inhomogeneity, and ECs.[86] These effects will produce additional phase and magnitude discontinuities between the echoes that generate spectral artifacts.

One widely used and effective method to tackle the ghost peaks is to separate the odd and even echoes in data processing. This method sacrifices half of the spectral bandwidth: however, sufficient bandwidth is typically retained to maintain the 10 ppm necessary at 3 T. When a limited bandwidth is problematic, Karczmar and coworkers have developed a method for combining the odd and even echoes that will maintain the spectral bandwidth and reduce spectral ghosts.[87] Both the reference NWS scans and WS scans have to be first separated into even and odd subsets and reorganized into $k_x - k_y - t_2 -$ (t_1 for WS only) matrices. In order to reduce the total scan time, NWS scans are taken with only a single t_1 point, which makes a 3D total data matrix, so only the WS matrix is 4D. Skewed squared SB apodization filters can be used to improve the spectral sensitivity as well as resolution.[37–39,52] Both data sets will then be subjected to 3D and 4D FFT reconstruction to produce two x-y-F_2-(F_1 for WS only) data matrices. The NWS EP-COSI/EP-JRESI data are used to determine the spatially-dependent resonant frequency shifts owing to local B_0 inhomogeneities and ECs from gradient switching. The corrections can be measured as the drift from the central frequency of the main water resonance, and compensated for by shifting the associated spectra of the WS EP-COSI/EP-JRESI data set. The even and odd echoes are combined by adding the complex subsets followed by FFT along the t_1 dimension.

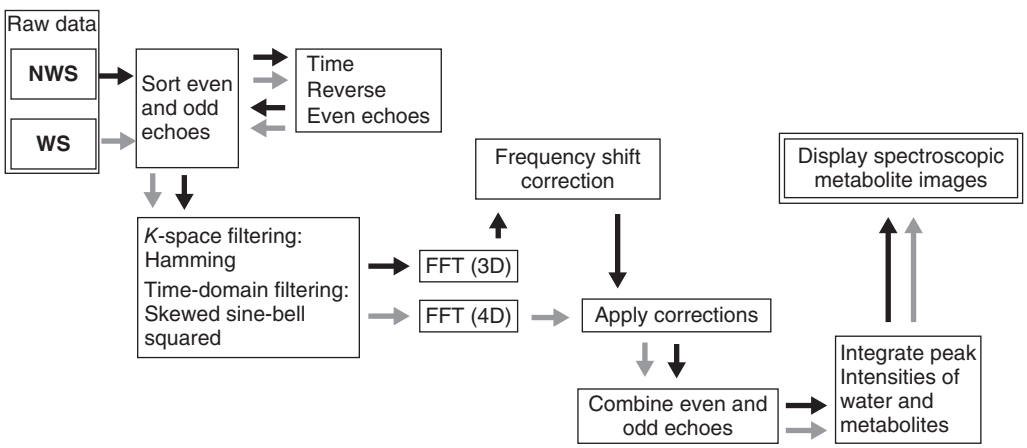

Figure 30.9. Reconstruction of the 4D EP-COSI/EP-JRESI datasets

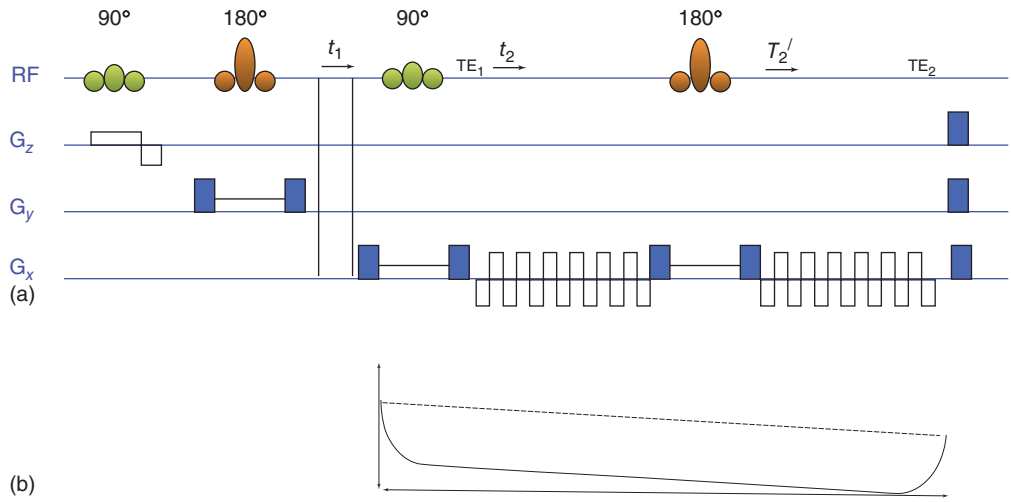

Figure 30.10. (a) The MEEP-COSI Pulse sequence diagram. (b) Diagram showing the effect of both T_2 (dashed line) and T_2* (solid line) on the overall shape of the signal envelope

30.3.5 Multiecho Echo-planar Correlated Spectroscopic Imaging (MEEP-COSI)

To record a turbo spin-echo (TSE) or fast spin-echo (FSE) MRI,[88–90] multiecho (ME)-encoding schemes have been used to reduce the overall scan duration dramatically. Similar ME-based techniques have shown greatly reduced scan times in MRSI and their applicability has already been demonstrated in 1D spectral-based MRSI, EP-JRESI, and correlated spectroscopic imaging[91–95] studies. A two-echo-based multiecho echo-planar correlated spectroscopic imaging (MEEP-COSI)[96] sequence (Figure 30.10) enables further acceleration (2×) of the EP-COSI sequence with only half of the acquisition time. In contrast to the 4D EP-COSI sequence, the 4D MEEP-COSI sequence refocuses the decaying magnetization during the initial readout train with a 180° RF pulse and samples a differently phase-encoded *k*-space line as the magnetization grows back until TE$_2$ during the second readout train within the same repetition time. The initial phase-encoding gradient is combined with the final spoiler gradient before the echo-planar readout. Following the first echo-planar readout (t_2), the initial phase encoding is reversed just before the 180° pulse, whereupon a different line in *k*-space is phase encoded after the 180° pulse.

Compared to the EP-COSI sequence, the repeated bipolar readout gradient creates two different sets of *k*-space trajectories that result in mirror images in real space. These two different sets of echoes can be summed together by time-reversing the even-numbered gradient echoes to create a single image. In a typical MEEP-COSI scan, 256 bipolar-gradient echo pair spectral signals are collected for each EPSI readout, yielding 256 t_2 points. 50 t_1 points are incrementally collected resulting in a scan time of 10 min, which is twice as fast as EP-COSI (20 min).[96]

30.3.6 Multiecho Echo-planar *J*-resolved Spectroscopic Imaging (MEEP-JRESI)

Furuyama *et al.*[93] first implemented the ME-based echo-planar spectroscopic imaging (ME-EPSI) on a 3 T MRI scanner and showed its application in human brain. Sarma *et al.*[95] modified the ME-EPSI sequence to implement ME-based echo-planar *J*-resolved Spectroscopic Imaging (MEEP-JRESI) in the human brain. At the core of the MEEP-JRESI sequence is the JPRESS module. To accelerate the acquisition, it employs two bipolar EPSI readouts separated by a slice-selective refocusing 180° pulse. After the last localization pulse, the first EPSI readout samples the magnetization starting at echo time, TE_1. After the completion of the first EPSI readout, the initial phase encoding is reversed, and the decaying magnetization

during the first readout train is refocused using the slice-selective 180° pulse. Subsequently, the second EPSI readout is used to measure the magnetization phase encoded to another line in *k*-space. In this way, two phase-encoding steps are accomplished within the same TR. A more detailed discussion on the implementation of multiecho, its effect on the point-spread function (PSF), and postprocessing steps to combine the two EPSI readouts can be found elsewhere (see also Chapter 12).[93]

A limiting factor for ME-based spectroscopic imaging is the T_2 decay, which diminishes the signal with each echo, and presents a potential problem in living tissue where T_2 relaxation times are shorter. This can be addressed by keeping the time between the different echoes as short as possible, although this limits the overall spectral resolution. Sarma *et al*. and Rajakumar *et al*. have successfully implemented the ME-EP-JRESI method in human brain and prostate, respectively.[95,97]

30.3.7 Data Processing of 4D MEEP-COSI/MEEP-JRESI

Reconstruction of the ME-EP-COSI/MEEP-JRESI data sets is done offline using a custom MATLAB software package as shown in Figure 30.11. Because of the opposite directions of the trajectories along k_x caused by the alternating readout gradients, the odd (or even) echoes must be reversed during data processing for reasons discussed in Section 30.3.4. Both the reference and water-suppressed scans will first be separated into positive (even) and negative (odd) subsets and reorganized into x-y-t_2-(t_1 for WS only) matrices. The reorganized spectral points will be interpolated to 1024 points using zero filling in the time domain (t_2). A skewed squared SB apodization filter can be used to reduce contamination from extra-voxel signals due to the imperfect PSF in both the non-water-suppressed and water-suppressed scans. Both data sets will then be subjected to 3D FFT reconstruction to produce two x-y-F_2-(F_1 for water suppressed only) data matrices.

30.3.8 Necessity of EC Correction in EP-COSI/EP-JRESI

As discussed in Section 30.2.3, the ECs can cause distortions in the spectra after FT and these distortions can

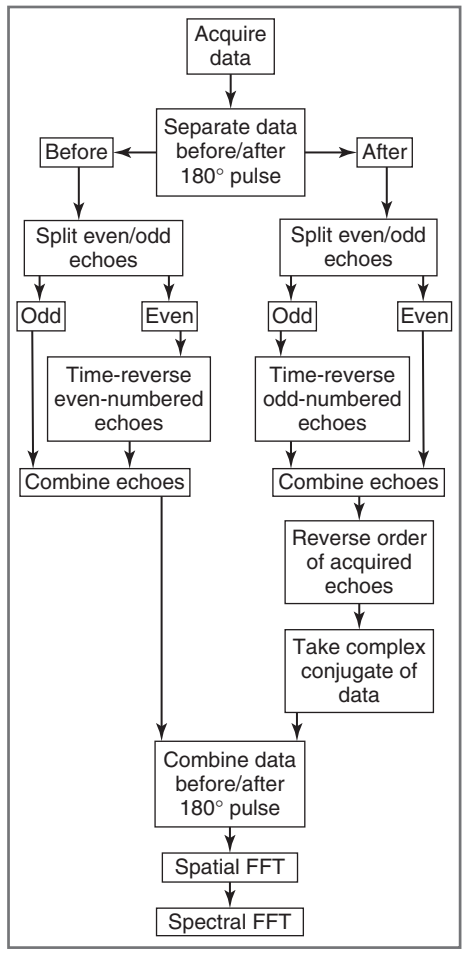

Figure 30.11. Different steps for postprocessing the MEEP-COSI/MEEP-JRESI datasets

be corrected in the WS scan using the phase differences measured from an NWS reference scan.[53–55] With the use of an EPSI readout, EC effects are greatly amplified and separate water reference scans or interleaved water reference scans are the norm for 1D spectroscopic imaging.[80,98] This is also the case when acquiring two spectral dimensions for spectroscopic imaging.

A pseudo 4D EP-COSI data recorded in a gray matter brain phantom (see Figure 30.4 caption) is considered here, using a sequence employing frequency encoding (k_x) only with one phase-encoding gradient along the other spatial dimension ($\Delta k_y = 0$) on a 3 T scanner. In this experiment, several columns are acquired instead of individual voxels in order to see the

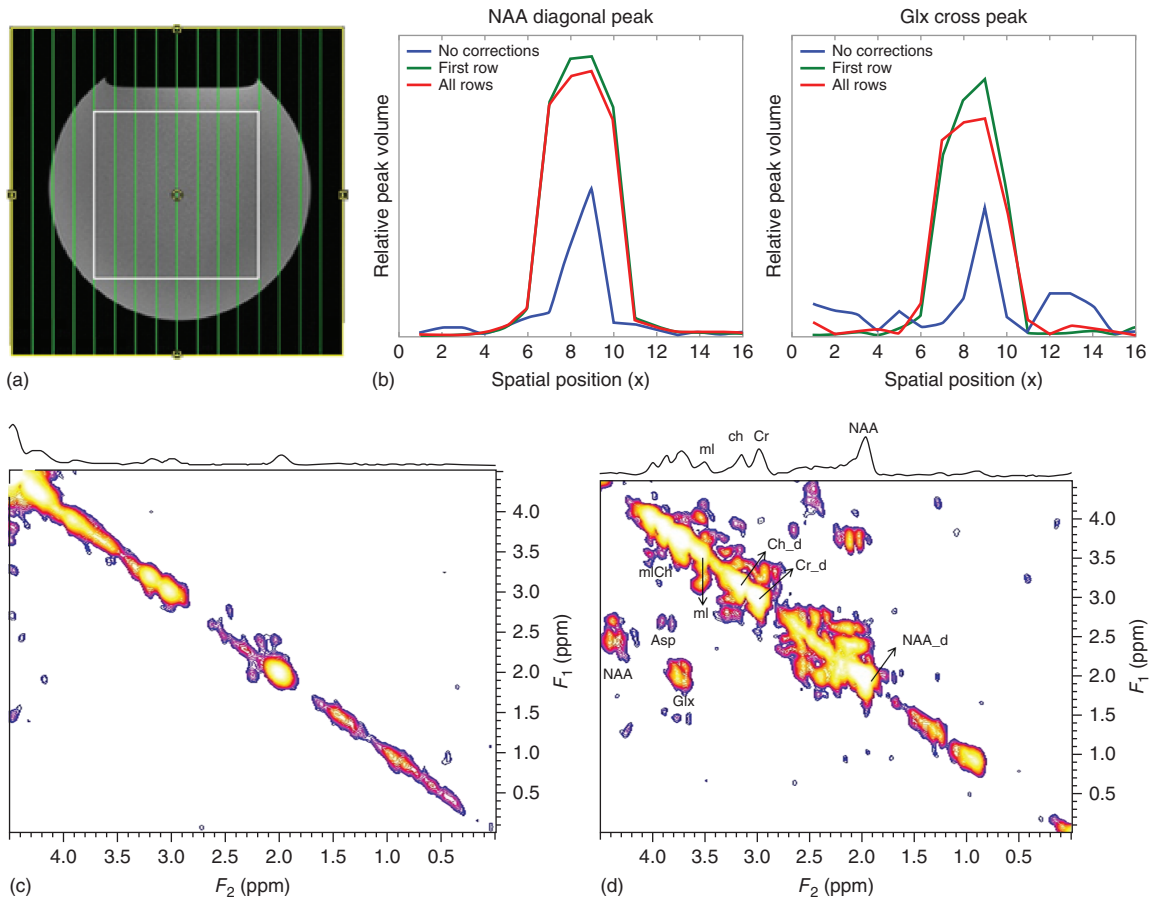

Figure 30.12. (a) Axial MRI of a phantom showing 16 vertical grids for EP-COSI with only one phase-encoding step ($\Delta k_y = 0$). (b) 1D spatial profiles of the NAA diagonal peak at 2 ppm (left) and glutamate/glutamine (Glx) cross-peaks (right) after postprocessing the EP-COSI data with and without EC corrections. The three colored curves represent three postprocessing methods: no EC corrections are applied (blue), EC corrections are applied only using the first NWS row (green), and EC corrections are applied using all t_1 NWS rows (red). (c) Extracted 2D COSY spectra from one of the columns without and (d) with EC (Klose's) correction

effects of the EC, as discussed in Section 30.2.3, on the spatial profile as evident in Figure 30.12(a). A reference NWS scan is also obtained with the same parameters. After data acquisition, the data are postprocessed in three different ways as discussed earlier (Figure 30.3): (i) using no corrections to the NWS data; (ii) using the first t_1 point for the EC[53]; and (iii) using all the t_1 points for EC correction. The difference between the second and third methods is that the second method does not correct the phase differences line by line, but instead uses the phase difference from the first line ($\Delta t_1 = 0$) and applies these changes to all successive lines ($\Delta t_1 > 0$). The second method is useful because an NWS scan with only a single t_1 point is necessary to perform the corrections, which greatly reduces scan time.[55]

Figure 30.12(b) shows the spatial profile along the echo-planar readout direction for the NAA diagonal peak as well as the Glx cross-peak. It is clear that not only the amplitudes of the diagonal peak and cross-peaks are affected by the EC, but the spatial profile as a whole is distorted too. It is interesting to note that the second correction method gives almost similar results to the third correction method and implies that the EC corrections do not greatly vary from t_1 point to t_1 point. Spectral quality of a central voxel

($x = 9$) is also greatly enhanced after the EC corrections, which can be seen by comparing the differences in Figure 30.12(c) and Figure 30.12(d). Without any corrections, the Glx and NAA cross-peaks are not qualitatively noticeable, whereas after corrections, the cross-peaks are apparent. Therefore, it is recommended that when performing multidimensional spectroscopic imaging (with 2 spectral + spatial dimensions), an NWS scan should be acquired with $\Delta t_1 = 0$ to use for EC corrections for higher spatial and spectral quality.

30.3.9 Application of 4D MEEP-JRESI in Human Brain

Sarma *et al.*[95] showed the feasibility of implementing MEEP-JRESI on human brain at 3 T. Figure 30.13 shows selected 2D *J*-resolved spectra extracted from a 4D MEEP-JRESI data set acquired from the mid-occipital and left temporal region of a healthy 59-year-old human brain. The peaks were localized within the PRESS excitation volume (Figure 30.13a; white box) with minimal leakage. 2D *J*-resolved spectra extracted from voxels in the left temporal and mid-occipital regions (Figure 30.13a; yellow and blue boxes) are shown in Figure 30.13(b) and (c). Both in the occipital and temporal lobes, Sarma *et al.* were able to quantify many metabolite resonances reliably, including cross-peaks due to J-coupling not observable with 1D MRS. In addition to the major metabolites, their results indicate stable estimation of important but minor metabolites such as Gln, Asp, PE, GSH, GABA, and Lac, which is particularly promising if it can allow a more accurate and reliable investigations of the roles these metabolites play in normal and disease states.

30.3.10 Evaluation of EP-COSI and MEEP-COSI in Calf Muscle

There has been significant attention focused on the relationships between lipid composition within the skeletal muscle and insulin sensitivity, diabetes and obesity. Determination of muscle triglycerides was classically only possible by invasive techniques.[99–102] In vivo spectra have been recorded in different regions of human skeletal muscle using SV 1D MRS with the VOI in the soleus, anterior tibialis, and other muscle regions, using the PRESS or STEAM SV

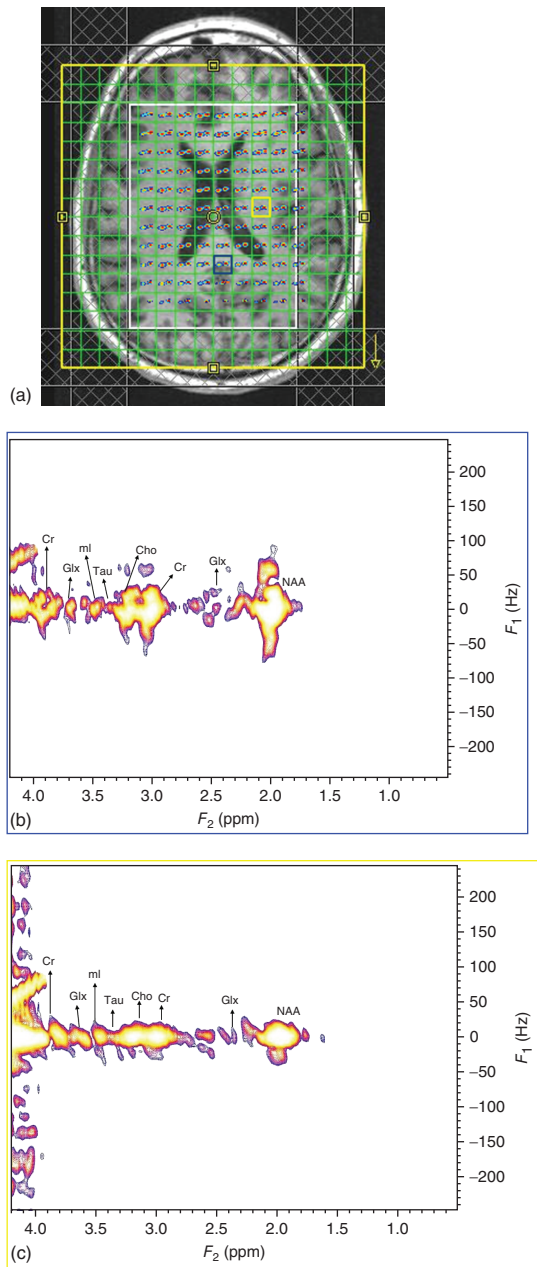

Figure 30.13. (a) Multivoxel spatial distribution of 2D diagonal peaks of Cr and Cho (3.0 and 3.2 ppm) overlaid on a T_1-weighted axial MRI. The white box indicates PRESS inner-volume localization, with voxels in the mid-occipital and left temporal lobes highlighted in blue and yellow, respectively. (b) Selected 2D *J*-resolved spectra extracted from the mid-occipital and (c) left temporal voxels

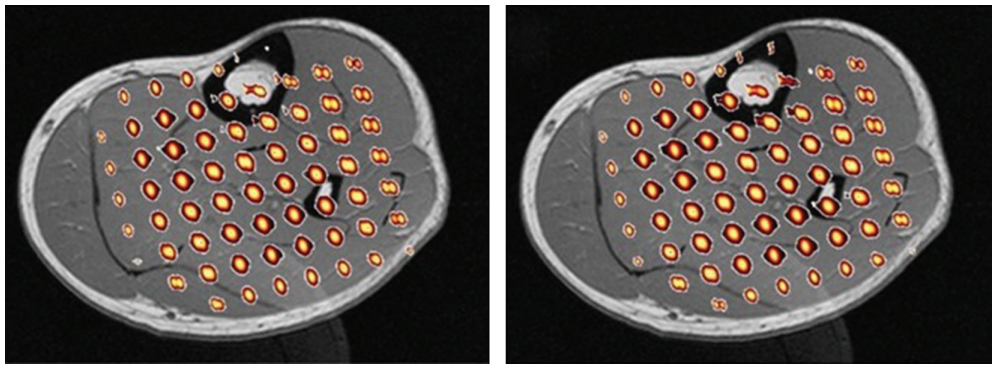

Figure 30.14. Comparison of the performance of the (a) MEEP-COSI and the (b) EP-COSI sequences in the calf of a healthy 28-year-old male volunteer. Spatial projections of the creatine diagonal peak at 3.9 ppm are overlaid on top of T_1-weighted axial MRI. (Reproduced with permission from Ref. 96. © John Wiley & Sons, Ltd., 2014)

sequences.[99,102–110] Spatially resolved MRS techniques enable quantitation of several metabolites including Cr, Cho groups, carnosine, etc. as well as intramyocellular lipids (IMCLs) and extramyocellular lipids (EMCLs).

As the IMCLs in muscle cells are stored in spheroid droplets adjacent to mitochondria, their proton density and concentration is larger than EMCLs, which are distributed over large regions of muscle fascia. Thus, the signal strength of IMCL is fairly constant, while the signal strength of EMCL may be affected by even a slight translocation of the voxel, so the challenge has been to develop appropriate, spatially efficient techniques that yield reproducible results. Li *et al.*[109] have compared MRSI and SV-MRS such as PRESS and STEAM techniques at 3 T and found that 2D MRSI showed better reproducibility for IMCL quantification than SV-MRS. It was also shown that both MRSI and SV-MRS methods have good reproducibility for measuring IMCL in vivo, but that MRSI offered greater flexibility, reliability, and higher sensitivity to IMCL differences, whereas a shorter scan time was possible with SV-MRS.[109] However, there is significant spectral overlap between the methyl groups of the saturated and unsaturated lipid signals in 1D MRS, which makes it difficult to distinguish and quantify these groups. In contrast, 2D L-COSY can clearly resolve the saturated and unsaturated peaks of IMCL and EMCL as well as those of metabolites such as Cr, Cho, and carnosine. This technique can provide a quantitative measure of the ratios of IMCL and EMCL, and saturated and unsaturated lipids in vivo.[44,83,111,112]

A major drawback of the SV-based 2D L-COSY[44,111,112] technique is that a larger voxel size (e.g., 27 cm^3) and longer acquisition time (>15 min) per VOI are typically required due to SNR limitations and the time required for the extra encoding. Hence, the acquisition of 2D L-COSY from multiple spatial locations can be very time consuming. Longer scan times demand system stability over a long duration and are less well tolerated by patients.

Figure 30.14 compares the performance of the 4D MEEP-COSI sequence with the 4D EP-COSI sequence. The images show spatial projections of the diagonal Cr peak at 3.9 ppm overlaid on top of a T_1-weighted axial MRI in the calf muscles of a healthy 28-year-old male volunteer.

Differences between the 2D spectra from soleus, tibialis anterior, and bone marrow from a 26-year-old healthy subject are shown in Figure 30.15. Figure 30.15(a) shows a T_1-weighted axial MRI annotated to highlight three voxels in the marrow, and in the tibialis and soleus muscles. The 2D COSY spectrum extracted from the soleus (Figure 30.15b) shows resonances in the muscle owing to the *N*-methyl and *N*-methylene protons of Cr(3.0 and 3.9 ppm), the trimethyl amine protons of Cho (3.20 ppm) and taurine (3.35 ppm), and the imidazole protons of carnosine (7.0 and 8.0 ppm), which are not present in the bone marrow (Figure 30.15b). In addition, the diagonal peaks of Cr (3.9 and 3.0 ppm) and other molecules in Figure 30.15(c) from the anterior tibialis show clear splitting due to residual dipole–dipole interactions. The MEEP-COSI data thus demonstrate discrimination of different tissues within the human calf. Similar

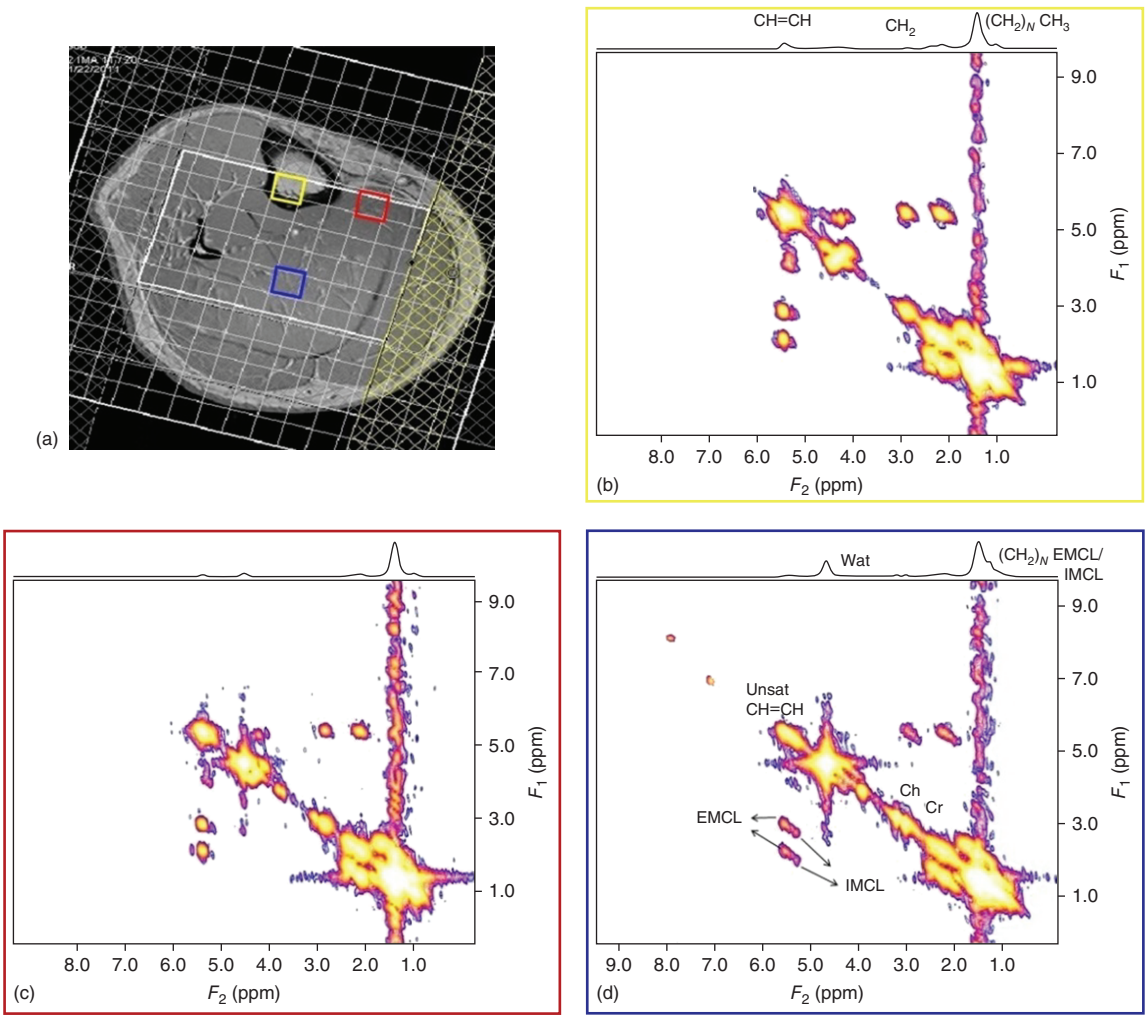

Figure 30.15. (a) T_1-weighted MRI of a human calf muscle in a 26-year-old healthy volunteer overlaid with an MRSI grid with voxels highlighted in the tibia marrow (yellow), tibialis anterior (red), and soleus (blue) muscles. 2D spectra with 1D diagonal projections (above) for (b) the marrow, (c) tibialis, and (d) soleus voxels

spectra can be obtained using EP-COSI in about 20 min of scan time.

30.4 ACCELERATED ECHO-PLANAR *J*-RESOLVED MRSI WITH NONUNIFORM UNDERSAMPLING AND COMPRESSED SENSING

Nonuniform undersampling (NUS) of *k*-space and subsequent reconstruction using compressed sensing (CS) are other ways to accelerate the scan time that have been successfully implemented in MRI and MRSI.[113–116] To implement CS successfully, the data should have a sparse representation in some transform domain and the aliasing artifacts produced by the NUS must be incoherent within the transform domain. The CS reconstruction attempts to enforce the sparsity, while simultaneously maintaining the fidelity of the original measurements to within the noise. Although CS has been used in standard CSI, its real advantage comes in multidimensional spectroscopic imaging employing echo-planar methods. Hu *et al.*[115] implemented NUS in hyperpolarized

^{13}C spectroscopic imaging along the spatial as well as spectral dimension using pseudo-random phase-encoding blips during the EPSI readout. Furuyama *et al*. and Sarma *et al*. successfully modified the 4D EP-JRESI sequence to accommodate NUS in the $k_y t_1$ plane,[84,116] while using the EPSI readout gradient to encode the spatial (k_x) and temporal dimensions (t_2). They achieved a twofold acceleration in scan time.

In both of these cases, an exponentially decaying sampling density scheme was used for NUS of the 4D EP-JRESI data. The sampling scheme was defined *as*

$$\eta(k_y, t_1) = \exp\left(-\frac{|k_y|}{a} - \frac{t_1}{b}\right) \tag{30.16}$$

where $\eta(k_y, t_1)$ is the probability that a data point is sampled, $-k_{y,\max} \le k_y \le k_{y,\max}$, $0 \le t_1 \le t_{1,\max}$, and a and b are flexible parameters that determine the acquired percentage of data. The CS method solves the constrained optimization problem[113]:

$$\arg\min_u \|\Psi u\|_1 \quad \text{s.t.} \quad \|F_p u - d\|_2^2 < \sigma \tag{30.17}$$

where u is the final reconstructed data, Ψ the sparsity transform, F_p the undersampled FT, d the sampled data, σ a fidelity factor, and $\|x\|_n$ the 'ℓ_n-norm'.

To implement EP-JRESI, Furuyama *et al*.[116] used the 'total variation' (TV) to enforce sparsity. The constrained problem in equation (30.17) is written as an unconstrained problem,

$$\arg\min_u TV(u) + \frac{\lambda}{2}\|F_p u - d\|_2^2 \tag{30.18}$$

where λ is a regularization parameter that weighs the sparsity against the data consistency, $u = R(x, y, F_1, F_2)$ is the final dataset, F_p is applied only along the y and F_1 dimensions, and $d = r(x, k_y, t_1, F_2)$ is the sampled data. The authors successfully implemented CS-based EP-JRESI in the prostates of healthy human volunteers, detecting the main metabolites citrate, Cr, spermine, Cho, etc.[116] They showed that CS reconstruction successfully cleans up the incoherent artifacts with fourfold undersampled data (one-fourth of the $k_y t_1$ points sampled) using two averages.

Sarma *et al*.[84] used CS-based EP-JRESI to investigate metabolic changes in multiple brain locations of obstructive sleep apnea (OSA) patients and healthy controls. Figure 30.16 shows extracted spectra from two voxels in medial frontal grey and dorsolateral prefrontal white matter regions after CS reconstruction of a fourfold undersampled in vivo brain scan (fourfold acceleration; two averages) together with the multivoxel display. Despite having only used 25% of the original data, the reconstructed data sets show alterations of metabolic features of OSA patients and healthy human brain[84] and demonstrate the clinical feasibility of a CS-based 4D EP-JRESI sequence.

Recently, NUS masking schemes and CS reconstruction have also been used to obtain a five-dimensional (5-D; k_x, k_y, k_z, t_2, t_1) in vivo brain acquisition in a clinically feasible scan time.[117] Normally this scan would take over 2–3 h, but using an eightfold acceleration factor allows a 21-min acquisition with $k_x = 16$, $k_y = 16$, $k_z = 8$, $t_2 = 256$, $t_1 = 64$, and TR = 1.2 s. Instead of utilizing an NUS scheme in the $k_y t_1$ plane, the nonuniform sampling is performed in the $k_y k_z t_1$ volume using the following sampling density function:

$$\eta(k_y, k_z, t_1) = \exp\left(-\frac{|k_y|}{a} - \frac{|k_z|}{a} - \frac{t_1}{c}\right) \tag{30.19}$$

where $\eta(k_y, k_z, t_1)$ is the probability a data point is sampled, $-k_{y,\max} \le k_y \le k_{y,\max}$, $-k_{z,\max} \le k_z \le k_{z,\max}$, $0 \le t_1 \le t_{1,\max}$, and *a, b,* and *c* are adjustable parameters that determine the sample weighting in each dimension. The data are reconstructed in the same manner that the 4D data are reconstructed, using either the ℓ_1-norm or TV-norm minimization [equations (30.17) and (30.18)]. However, these optimizations must also account for the extra dimension, which increases computation time by an order of magnitude.

Wilson *et al*.[117] showed that despite using higher acceleration factors (eightfold), peak integrals of major brain metabolites including NAA, Glx, Cr, Cho, and mI show high reproducibility in vivo. In phantom studies, these same metabolites show very low peak root-mean-square errors (RMSEs), implying that the peaks are properly reconstructed. As this is a novel technique, further validation studies must be conducted and its potential applications in different pathologies determined.[118]

30.5 PRIOR-KNOWLEDGE FITTING FOR METABOLITE QUANTITATION

A few years ago, Schulte *et al*. developed a prior-knowledge fitting (ProFit) algorithm based on a linear combination of 2D model spectra and demonstrated the feasibility of quantification of brain and prostate metabolites (see Chapter 20).[34,61,119,120] Unlike the 1D MRS fitting algorithms such as LC

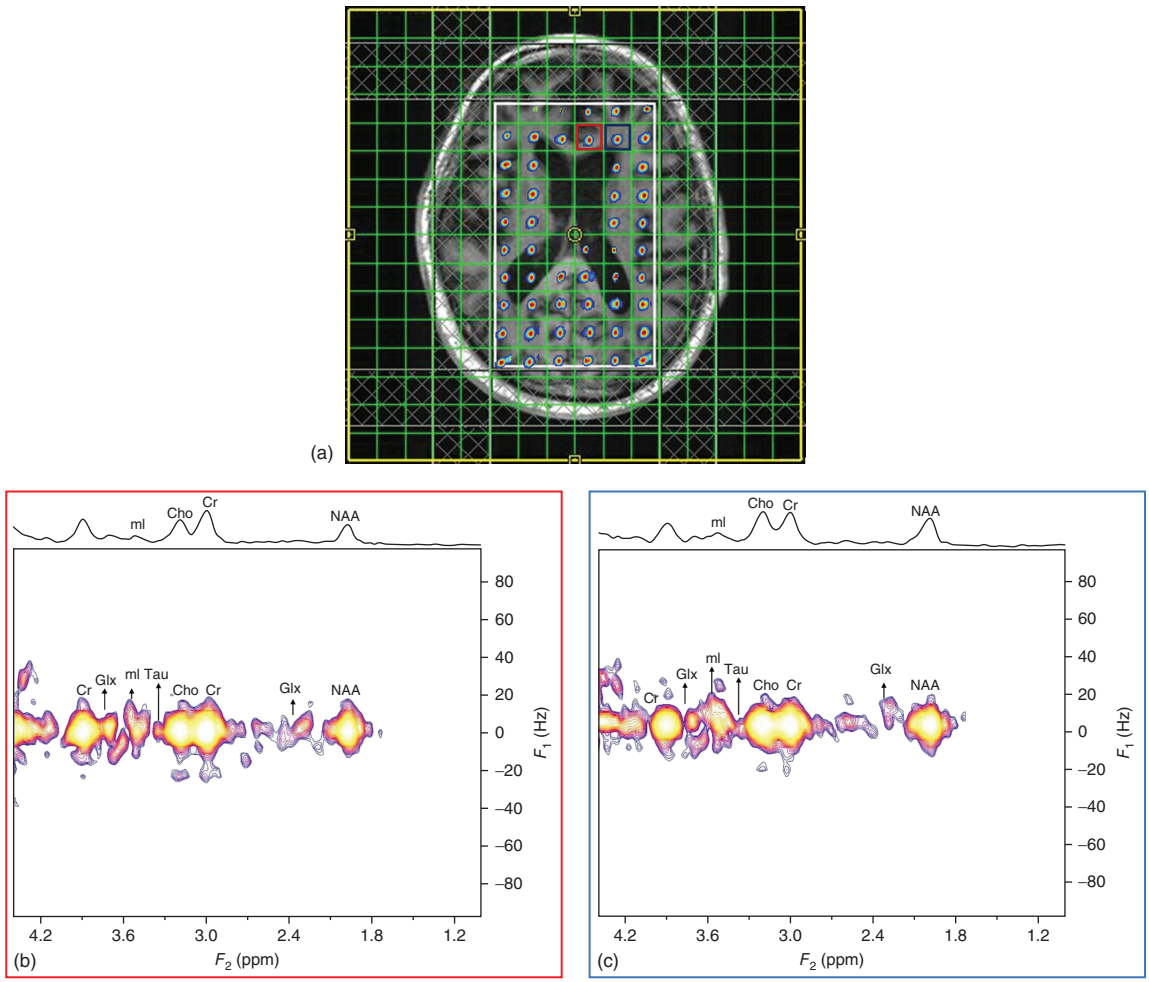

Figure 30.16. Reconstruction of an undersampled 4D EP-JRESI in vivo brain scan of a 69-year-old OSA patient with only 25% of the samples (as required by the Nyquist–Shannon criterion). (a) An MRSI GRID with the diagonal NAA peaks overlaid on top of a T_1-weighted axial MRI. The white box indicating the PRESS inner-volume localization, containing voxels highlighted in the mid-frontal (red) and left-frontal (blue) brain. The corresponding 2D *J*-resolved spectra extracted from the mid-frontal and left-frontal voxels are shown in (b) and (c), respectively. (Reproduced with permission from Ref. 84. © American Society of Neuroradiology, 2014)

model and JMRUI,[4,5] ProFit performs a hybrid time- and frequency-domain fitting using a nonlinear outer loop and an inner linear least-squares fit for obtaining signal amplitudes (proportional to the concentrations) and incorporates the maximum available prior knowledge. Before fitting the data, zeroth-order phase correction and frequency shifts in F_1 and F_2 dimensions are applied to the extracted 2D spectra. After the fitting process, the quality of the fit can be individually evaluated for each metabolite using Cramer–Rao lower bounds (CRLB) criteria.[121] A statistical lower bound for the achievable standard deviation of the estimated parameters is provided by CRLB, which is not dependent on the individual signal intensities but only on the noise and the orthogonality of the basis function. The architecture of the fitting process allows for another useful measure of the quality of the fitting of the spectrum by comparing the creatine 3.9 ppm (Cr3.9) to the creatine 3.0 ppm (Cr3.0) signal ratio, which ideally should be 1 because

the number of protons (2 and 3, respectively) is already accounted for in their prior-knowledge basis set. Higher Cr3.9/Cr3.0 ratios reflect poor or suspect spectra that may provide grounds for excluding a data set. Note that in order to implement this control, Cr3.9 and Cr3.0 have to be entered as separate elements in the basis sets. Our preliminary results using ProFit quantitation of previously acquired GE 1.5 T, and Siemens 3 T and 1.5 T 2D L-COSY data acquired from several brain pathologies, has demonstrated an improved ability for estimating more brain metabolites such as GSH, phosphocholine (PCh), phosphoethanolamine (PE), and glycerophosphocholine.[35,45] However, the applicability of ProFit in a clinical setting and multisite testing is yet to be demonstrated.

30.6 FUTURE DIRECTIONS: CLINICAL APPLICATIONS

Localized 2D MRS has left its infancy and is maturing. In contrast to the decades-old SV-based 2D L-COSY and 2D JPRESS spectroscopic sequences, fully-sampled multivoxel-based 4D EP-JRESI and EP-COSI sequences facilitate the recording of 2D COSY and *J*-resolved spectra from multiple regions of the brain. In past, lengthy scan times of approximately 20–40 min and longer have also been a major impediment to clinical 2D MRS, depending on the number of steps for the incremented spectral- (t_1) and spatial-encoding (k_y) dimensions. Now, recent developments demonstrate that further acceleration is possible using NUS schemes, the end result being the shortening of the total scan time for 4D EP-JRESI and EP-COSI sequences to around 10 min or less. Postprocessing of 4D and 5-D NUS data using the nonlinear CS reconstruction schemes such as ℓ_1-norm-minimization, maximum entropy, and group sparsity is required.

The inclusion of adiabatic RF pulses into the multidimensional MRSI sequences has been a recent interest and different versions of sLASER-based 4D and 5-D EP-COSI/EP-JRESI sequences are currently being investigated for more reliable and quantitative detection of metabolites in the whole brain, other organs, and glands. Future efforts will undoubtedly focus on demonstrating the clinical potential of multidimensional MRSI using fast imaging methods including those described herein. It is our hope that all these recent developments will lead to clinical value for these novel MRSI sequences and create a new paradigm for noninvasive clinical investigation of normal and diseased states. At the very least, these techniques clearly demonstrate a rich treasure trove of information linking molecules, metabolism, and function that awaits our investigation.

ACKNOWLEDGMENTS

The authors would like to acknowledge the scientific support of Dr. Jonathan Furuyama, Mr. Neil Wilson and Dr. Brian Burns with the NUS-based acquisition schemes and postprocessing using CS algorithms. Also this work was supported by National Institute of Health [R21NS080649 (MAT), R21NS086449 (RN), R01NR013693 (PMM)] and CDMRP Prostate and Breast Cancer Research Programs (#W81XWH-11-1-0248 and W81XWH-10-1-0743, MAT)].

REFERENCES

1. M. Van der-Graaf, *Eur. Biophys. J.*, 2010, **39**, 527. Epub 2009 Aug 13.
2. J. H. Hwang and H. S. Choi, *Exp. Mol. Med.*, 2015, **47**, e139.
3. G. Oz, J. R. Alger, P. B. Barker, R. Bartha, A. Bizzi, C. Boesch, P. J. Bolan, K. M. Brindle, C. Cudalbu, A. Dinçer, U. Dydak, U. E. Emir, J. Frahm, R. G. González, S. Gruber, R. Gruetter, R. K. Gupta, A. Heerschap, A. Henning, H. P. Hetherington, F. A. Howe, P. S. Hüppi, R. E. Hurd, K. Kantarci, D. W. Klomp, R. Kreis, M. J. Kruiskamp, M. O. Leach, A. P. Lin, P. R. Luijten, M. Marjańska, A. A. Maudsley, D. J. Meyerhoff, C. E. Mountford, S. J. Nelson, M. N. Pamir, J. W. Pan, A. C. Peet, H. Poptani, S. Posse, P. J. Pouwels, E. M. Ratai, B. D. Ross, T. W. Scheenen, C. Schuster, I. C. Smith, B. J. Soher, I. Tkáč, D. B. Vigneron, R. A. Kauppinen, and MRS Consensus Group, *Radiology*, 2014, **270**, 658.
4. S. W. Provencher, *NMR Biomed.*, 2001, **14**, 260.
5. A. Naressi, C. Couturier, I. Castang, R. de Beer, and D. Graveron-Demilly, *Comput. Biol. Med.*, 2001, **31**, 269.
6. J. Pfeuffer, I. Tkac, S. W. Provencher, and R. Gruetter, *J. Magn. Reson.*, 1999, **141**, 104.
7. N. Puts and R. A. E. Edden, *Prog. Nucl. Magn. Reson. Spectrosc.*, 2012, **60**, 29.
8. K. Wakamatsu, H. Tanaka, K. Tabuchi, M. Ojika, F. A. Zucca, L. Zecca, and S. Ito, *Molecules*, 2014, **19**, 8039.

9. J. M. Duarte, K. Q. Do, and R. Gruetter, *Neurobiol. Aging*, 2014, **35**, 1660. Epub 2014 Jan 31.
10. A. M. Weber, N. Soreni, and M. D. Noseworthy, *MAGMA*, 2014, **27**, 291. Epub 2013 Nov 28.
11. M. A. Thomas, R. Nagarajan, A. Huda, D. Margolis, M. K. Sarma, K. Sheng, R. E. Reiter, and S. S. Raman, *NMR Biomed.*, 2014, **27**, 53. Epub 2013 Jul 31.
12. M. A. Thomas, A. Huda, H. K. Chung, N. Binesh, T. Venkatraman, A. Ambrosio, and S. Banakar, *Modern Magn. Reson.*, 2006, 1171. Webb G.A. (ed.).
13. M. Marjańska, E. J. Auerbach, R. Valabrègue, P. F. Van de Moortele, G. Adriany, and M. Garwood, *NMR Biomed.*, 2012, **25**, 332. Epub 2011 Jul 27.
14. D. L. Rothman, O. A. Petroff, K. L. Behar, and R. H. Mattson, *Proc. Natl. Acad. Sci. U. S. A.*, 1993, **90**, 5662.
15. L. An, Y. Zhang, D. M. Thomasson, L. L. Latour, E. H. Baker, J. Shen, and S. Warach, *J. Magn. Reson. Imaging*, 2009, **30**, 263.
16. W. Bogner, S. Gruber, M. Doelken, A. Stadlbauer, O. Ganslandt, U. Boettcher, S. Trattnig, A. Doerfler, H. Stefan, and T. Hammen, *Eur. J. Radiol.*, 2010, **73**, 526. Epub 2009 Feb 7.
17. C. J. Evans, N. A. Puts, S. E. Robson, F. Boy, D. J. McGonigle, P. Sumner, K. D. Singh, and R. A. Edden, *J. Magn. Reson. Imaging*, 2013, **38**, 970. Epub 2012 Nov 27.
18. M. Mescher, H. Merkle, J. Kirsch, M. Garwood, and R. Gruetter, *NMR Biomed.*, 1998, **11**, 266.
19. P. Bottomley, *Ann. N. Y. Acad. Sci.*, 1987, **508**, 333.
20. J. Frahm, H. Bruhn, M. L. Gyngell, K. D. Merboldt, W. Hänicke, and R. Sauter, *Magn. Reson. Med.*, 1989, **9**, 79.
21. M. Craveiro, C. Cudalbu, V. Mlynárik, and R. Gruetter, *NMR Biomed.*, 2014, **27**, 1151. Epub 2014 Jul 29.
22. A. Andreychenko, V. O. Boer, C. S. Arteaga de Castro, P. R. Luijten, and D. W. Klomp, *Magn. Reson. Med.*, 2012, **68**, 1018. Epub 2011 Dec 28.
23. W. Nosel, L. A. Trimble, J. F. Shen, and P. S. Allen, *Magn. Reson. Med.*, 1989, **11**, 398.
24. M. A. Thomas, H. P. Hetherington, D. J. Meyerhoff, and D. B. Twieg, *J. Magn. Reson.*, 1991, **93**, 485.
25. T. R. Brown, B. M. Kincaid, and K. Ugurbil, *Proc. Natl. Acad. Sci. U. S. A.*, 1982, **79**, 3523.
26. P. A. Bottomley, H. C. Charles, P. B. Roemer, D. Flamig, H. Engeseth, W. A. Edelstein, and O. M. Mueller, *Magn. Reson. Med.*, 1988, **7**, 319.
27. S. Posse and W. P. Aue, *NMR Biomed.*, 1989, **2**, 234.
28. P. R. Luyten, A. J. Marien, W. Heindel, P. H. van Gerwen, K. Herholz, J. A. den Hollander, G. Friedmann, and W. D. Heiss, *Radiology*, 1990, **176**, 791.
29. V. Govind, S. Gold, K. Kaliannan, G. Saigal, S. Falcone, K. L. Arheart, L. Harris, J. Jagid, and A. A. Maudsley, *J. Neurotrauma*, 2010, **27**, 483.
30. J. M. Lupo and S. J. Nelson, *Semin. Radiat. Oncol.*, 2014, **24**, 248. Epub 2014 Jul 26.
31. L. N. Ryner, J. A. Sorenson, and M. A. Thomas, *J. Magn. Reson. B*, 1995, **107**, 126.
32. L. N. Ryner, J. A. Sorenson, and M. A. Thomas, *Magn. Reson. Imaging*, 1995, **13**, 853.
33. R. Kreis and C. Boesch, *J. Magn. Reson.*, 1996, **B113**, 103.
34. R. F. Schulte and P. Boesiger, *NMR Biomed.*, 2006, **19**, 255.
35. M. K. Sarma, A. Huda, R. Nagarajan, C. H. Hinkin, N. Wilson, R. K. Gupta, E. Frias-Martinez, J. Sayre, B. Guze, S. H. Han, and M. A. Thomas, *Metab. Brain Dis.*, 2011, **26**, 173.
36. A. Fuchs, P. Boesiger, R. F. Schulte, and A. Henning, *Magn. Reson. Med.*, 2013. Epub ahead of print.
37. W. P. Aue, E. Bartholdi, and R. R. Ernst, *J. Chem. Phys.*, 1976, **64**, 2229.
38. M. A. Thomas, K. Yue, N. Binesh, P. Davanzo, A. Kumar, B. Siegel, M. Frye, J. Curran, R. Lufkin, P. Martin, and B. Guze, *Magn. Reson. Med.*, 2001, **46**, 58.
39. N. Binesh, K. Yue, L. Fairbanks, and M. A. Thomas, *Magn. Reson. Med.*, 2002, **48**, 942.
40. M. A. Thomas, N. Hattori, U. Umeda, T. Sawada, and S. Naruse, *NMR Biomed.*, 2003, **16**, 245.
41. S. Banakar, N. Wyckoff, A. Huda, A. Marumoto, and S. Raman, *Spectroscopy*, 2003, **17**, 521.
42. N. Binesh, A. Huda, M. Bugbee, R. Gupta, N. Rasgon, A. Kumar, M. Green, S. Han, and M. A. Thomas, *J. Magn. Reson. Imaging*, 2005, **21**, 398.
43. M. A. Thomas, T. Lange, S. S. Velan, R. Nagarajan, S. Raman, A. Gomez, D. Margolis, S. Swart, R. R. Raylman, R. F. Schulte, and P. Boesiger, *MAGMA*, 2008, **21**, 443.
44. P. Srikanthan, A. Singhal, C. C. Lee, R. Nagarajan, N. Wilson, C. K. Roberts, T. J. Hahn, and M. A. Thomas, *Magn. Reson. Insights*, 2012, **5**, 29.
45. R. Nagarajan, M. K. Sarma, A. D. Thames, S. A. Castellon, C. H. Hinkin, and M. A. Thomas, *Int. J. Hepatol.*, 2012, **2012**, 179365.

46. G. Verma, H. Hariharan, R. Nagarajan, R. P. Nanga, E. J. Delikatny, M. Albert Thomas, and H. Poptani, *J. Magn. Reson. Imaging*, 2014, **40**, 1319. Epub 2013 Nov 22.
47. O. W. Sorensen, G. W. Eich, M. H. Levitt, G. Bodenhausen, and R. R. Ernst, *Prog. NMR Spectrosc.*, 1983, **16**, 163.
48. I. M. Brereton, G. J. Galloway, S. E. Rose, and D. M. Doddrell, *Magn. Reson. Med.*, 1994, **32**, 251.
49. R. R. Ernst, G. Bodenhausen, and A. Wokaun, Principles of NMR Spectroscopy in One and Two Dimensions, Oxford Publications: Oxford, 1987, 283.
50. M. H. Levitt, Spin Dynamics: Basics of Nuclear Magnetic Resonance, John Wiley & Sons, Ltd: Chichester, UK, 2002, 361.
51. J. Keeler, Understanding NMR Spectroscopy, John Wiley & Sons: Cambridge, UK, 2002.
52. E. J. Delikatny, W. E. Hull, and C. E. Mountford, *J. Magn. Reson.*, 1991, **94**, 563.
53. U. Klose, *Magn. Reson. Med.*, 1990, **14**, 26.
54. F. Jiru, *Eur. J. Rad.*, 2008, **67**, 202.
55. H. Watanabe, N. Takaya, and F. Mitsumori, *Magn. Reson. Med. Sci.*, 2013, **12**, 215.
56. S. Banakar, T. N. Venkatraman, K. Yue, N. Binesh, and M. A. Thomas, In *Proceedings of International Conference on Mathematics and Engineering Techniques in Medicine and Biological Sciences*. June 24–27, 2002, pp. 500–504.
57. K. Nagayama, K. Wuthrich, and R. R. Ernst, *Biochem. Biophys. Res. Commun.*, 1979, **90**, 305.
58. N. Binesh, K. Yue, and M. A. Thomas, *Proc. Intl. Soc. Mag. Reson. Med.*, 2000, **8**, 1864.
59. M. A. Thomas, L. N. Ryner, M. P. Mehta, P. A. Turski, and J. A. Sorenson, *J. Magn. Reson. Imaging*, 1996, **6**, 453.
60. K. Yue, A. Marumoto, N. Binesh, and M. A. Thomas, *Magn. Reson. Med.*, 2002, **47**, 1059.
61. R. F. Schulte, T. Lange, J. Beck, D. Meier, and P. Boesiger, *NMR Biomed.*, 2006, **19**, 264.
62. S. Macura and L. R. Brown, *J. Magn. Reson.*, 1983, **53**, 529.
63. M. G. Swanson, D. B. Vigneron, T. K. Tran, N. Sailasuta, R. E. Hurd, and J. Kurhanewicz, *Magn. Reson. Med.*, 2001, **45**, 973.
64. P. J. Bolan, L. DelaBarre, E. H. Baker, H. Merkle, L. I. Everson, D. Yee, and M. Garwood, *Magn. Reson. Med.*, 2002, **48**, 215.
65. M. Garwood and L. DelaBarre, *J. Magn. Reson.*, 2001, **153**, 155.
66. T. W. Scheenen, D. W. Klomp, J. P. Wijnen, and A. Heerschap, *Magn. Reson. Med.*, 2008, **59**, 1.
67. T. W. Scheenen, A. Heerschap, and D. W. Klomp, *MAGMA*, 2008, **21**, 95.
68. J. Mao, T. H. Mareci, and E. R. Andrew, *J. Magn. Reson.*, 1988, **79**, 1.
69. J. Pauly, D. Nishimura, and A. Macovski, *J. Magn. Reson.*, 1989, **81**, 43.
70. D. Nishimura and A. Macovski, *J. Magn. Reson.*, 1989, **82**, 571.
71. R. V. Mulkern and J. L. Bowers, *Concepts Magn. Reson.*, 1994, **6**, 1.
72. J. Slotboom, A. F. Mehlkopf, and W. M. M. J. Bovee, *J. Magn. Reson.*, 1991, **95**, 396.
73. A. Allerhand, *J. Chem. Phys.*, 1966, **44**, 1.
74. S. Ramadan and C. Mountford, *J. Magn. Reson. Imaging*, 2011, **33**, 1447.
75. M. Lin, A. Kumar, and S. Yang, *Magn. Reson. Med.*, 2014, **72**, 26. Epub 2013 Oct 1.
76. M. Lin, A. Kumar, and S. Yang, *Magn. Reson. Med.*, 2014, **71**, 911.
77. P. Mansfield, *J. Phys. D Appl. Phys.*, 1983, **16**, L235.
78. P. Mansfield, *Magn. Reson. Med.*, 1984, **1**, 370.
79. S. Matsui, K. Sekihara, and H. Kohno, *J. Magn. Reson.*, 1986, **67**, 476.
80. S. Posse, C. DeCarli, and D. Le-Bihan, *Radiology*, 1994, **192**, 733.
81. S. Posse, G. Tedeschi, R. Risinger, R. Ogg, and D. Le-Bihan, *Magn. Reson. Med.*, 1995, **33**, 34.
82. A. Ebel, B. Soher, and A. Maudsley, *Magn. Reson. Med.*, 2001, **46**, 1072.
83. S. Lipnick, G. Verma, S. Ramadan, J. Furuyama, and M. Thomas, *Magn. Reson. Med.*, 2010, **64**, 947.
84. M. K. Sarma, R. Nagarajan, P. M. Macey, R. Kumar, J. P. Villablanca, J. Furuyama, and M. A. Thomas, *Am. J. Neuroradiol.*, 2014, **35**, S81.
85. Nagarajan R, Furuyama J, Margolis D, S. Raman, M. K. Sarma, and M. A. Thomas, Echo Planar based J Resolved and Correlated Spectroscopic Imaging of Human Prostate Using External Coil, 2011. Published online at www.ismrm.org, Abstract 2801.
86. P. Jezzard, A. S. Barnett, and C. Pierpaoli, *Magn. Reson. Med.*, 1998, **39**, 801.

87. W. Du, Y. P. Du, X. Fan, M. A. Zamora, and G. S. Karczmar, *Magn. Reson. Med.*, 2003, **49**, 1113.
88. J. Hennig, A. Nauerth, and H. Friedburg, *Magn. Reson. Med.*, 1986, **3**, 823.
89. R. Constable, R. Smith, and J. Gore, *J. Comput. Assist Tomogr.*, 1992, **16**, 41.
90. J. Listerud, S. Einstein, E. Outwater, and H. Y. Kressel, *Magn. Reson. Q.*, 1992, **8**, 199.
91. J. H. Duyn and C. T. W. Moonen, *Magn. Reson. Med.*, 1993, **30**, 409.
92. U. Dydak, D. Meier, R. Lamerichs, and P. Boesiger, *Am. J. Neuroradiol.*, 2006, **27**, 1441.
93. J. K. Furuyama, B. L. Burns, N. E. Wilson, and M. A. Thomas, *Materials*, 2011, **4**, 1818.
94. G. Verma, S. Lipnick, S. Ramadan, R. Nagarajan, and M. A. Thomas, *J. Magn. Reson. Imaging*, 2011, **34**, 262.
95. M. K. Sarma, R. Nagarajan, N. Wilson, J. K. Furuyama, and M. A. Thomas, *Proc. Int. Soc. Mag. Reson. Med.*, 2012, **20**, Abstract 4462.
96. J. K. Furuyama, R. Nagarajan, C. K. Roberts, C. C. Lee, T. J. Hahn, and M. A. Thomas, *NMR Biomed.*, 2014, **27**, 1176.
97. R. Nagarajan, J. Furuyama, M. K. Sarma, D. J. Margolis, S. S. Raman, R. Reiter, and M. A. Thomas. Multi-Echo EP-based J-resolved Magnetic Resonance Spectroscopic Imaging of Prostate Cancer, 2011. Published online at www.rsna2011.rsna.org, Abstract 186.
98. A. Ebel and A. A. Maudsley, *Magn. Reson. Med.*, 2005, **53**, 465.
99. S. Sinha, M. Rathi, A. Misra, V. Kumar, M. Kumar, N. R. Jagannathan, R. M. Pandey, M. Dwivedi, and K. Luthra, *Clin. Endocrinol. (Oxf)*, 2005, **63**, 350.
100. D. A. Pan, S. Lillioja, A. D. Kriketos, M. R. Milner, L. A. Baur, C. Bogardus, A. B. Jenkins, and L. H. Storlien, *Diabetes*, 1997, **46**, 983.
101. K. Levin, H. D. Schroeder, F. P. Alford, and H. Beck-Nielsen, *Diabetologia*, 2001, **44**, 824.
102. M. Torriani, B. J. Thomas, E. F. Halpern, M. E. Jensen, D. I. Rosenthal, and W. E. Palmer, *Radiology*, 2005, **236**, 609.
103. C. Boesch, J. Machann, P. Vermathen, and F. Schick, *NMR Biomed.*, 2006, **19**, 968.
104. B. H. Goodpaster, R. Theriault, S. C. Watkins, and D. E. Kelley, *Metabolism*, 2000, **49**, 467.
105. J. He, S. Watkins, and D. E. Kelley, *Diabetes*, 2001, **50**, 817.
106. F. Schick, B. Eismann, W.-I. Jung, H. Bongers, M. Bunse, and O. Lutz, *Magn. Reson. Med.*, 1993, **29**, 158.
107. C. Boesch, J. Slotboom, H. Hoppeler, and R. Kreis, *Magn. Reson. Med.*, 1997, **37**, 484.
108. L. S. Szczepaniak, E. E. Babcock, F. Schick, R. L. Dobbins, A. Garg, D. K. Burns, J. D. McGarry, and D. T. Stein, *Am. J. Physiol.*, 1999, **276**, E977.
109. X. Li, J. F. Youngren, B. Hyun, G. K. Sakkas, K. Mulligan, S. Majumdar, U. B. Masharani, M. Schambelan, and I. D. Goldfine, *Magn. Reson. Imaging*, 2008, **26**, 188.
110. G. D. Wells, M. D. Noseworthy, J. Hamilton, M. Tarnopolski, and I. Tein, *Can. J. Neurol. Sci.*, 2008, **35**, 31.
111. S. S. Velan, C. Durst, S. K. Lemieux, R. R. Raylman, R. Sridhar, R. G. Spencer, G. R. Hobbs, and M. A. Thomas, *J. Magn. Reson. Imaging*, 2007, **25**, 192.
112. S. S. Velan, N. Said, C. Durst, S. Frisbee, J. Frisbee, R. R. Raylman, M. A. Thomas, V. M. Rajendran, R. G. Spencer, and S. E. Alway, *Am. J. Physiol. Regul. Integr. Comp. Physiol.*, 2008, **295**, R1060.
113. D. Donoho, *IEEE Trans. Info. Theory*, 2006, **52**, 1289.
114. M. Lustig, D. Donoho, and J. M. Pauly, *Magn. Reson. Med.*, 2007, **58**, 1182.
115. S. Hu, M. Lustig, A. Chen, J. Crane, A. Kerr, D. Kelley, R. Hurd, J. Kurhanewicz, S. Nelson, J. Pauly, and D. Vigneron, *J. Magn. Reson.*, 2008, **192**, 258.
116. J. Furuyama, N. Wilson, B. Burns, R. Nagarajan, D. J. Margolis, and M. A. Thomas, *Magn. Reson. Med.*, 2012, **67**, 1499.
117. N. E. Wilson, Z. Iqbal, B. L. Burns, M. Keller, and M. A. Thomas, *Magn. Reson. Med.*, 2016, **75**, 42.
118. N. E. Wilson, B. L. Burns, Z. Iqbal, and M. A. Thomas, *Magn. Reson. Med.*, 2015, **74**, 1199.
119. T. Lange, R. F. Schulte, and P. Boesiger, *Magn. Reson. Med.*, 2008, **59**, 966.
120. M. A. Thomas, T. Lange, S. S. Velan, R. Nagarajan, S. Raman, A. Gomez, D. Margolis, S. Swart, R. R. Raylman, R. F. Schulte, and P. Boesiger, *Magn. Reson. Mater. Phys. Biol. Med.*, 2008, **21**, 443.
121. S. Cavassila, S. Deval, C. Huegen, D. van Ormondt, and D. Graveron-Demilly, *J. Magn. Reson.*, 2000, **143**, 311.